On the generation of large-scale eddy-driven patterns: the average eddy model

Timour Radko†

Department of Oceanography, Naval Postgraduate School, Monterey, CA 93943, USA

A theoretical model is developed which illustrates the dynamics of the spontaneous generation of large-scale structures in baroclinically unstable eddying flows. Techniques of asymptotic multiscale analysis are used to identify instabilities resulting from the positive feedback of the background eddies on large-scale perturbations. The novelty of the proposed approach lies in the choice of a dynamically consistent time-dependent background eddy field, which is taken from simulations of baroclinic instability in the Phillips two-layer system. The resulting solutions differ considerably from those of traditional multiscale models, in which the background eddy field is represented by steady analytical patterns. The present formulation makes it possible to (i) test the multiscale theory against the corresponding numerical simulations, (ii) unambiguously interpret the key physical processes at play and (iii) rationalize the emergence of large-scale patterns for certain background parameters. While the proposed approach to multiscale modelling is illustrated on a particular example of the Phillips baroclinic instability model, it is our belief that the presented technique is readily adaptable to a wide range of applications.

Key words: geophysical and geological flows, instability

1. Introduction

While the broad oceanographic significance of the eddy-induced transport of buoyancy, momentum and energy has been firmly established (Robinson 1983; Kamenkovich, Koshlyakov & Monin 1986), specific mechanisms of the interaction between mesoscale variability and large-scale circulation patterns are still poorly understood and quantified. The nonlinear evolution of eddies in the ocean is a complex multiscale and multistage process. Unstable waves emerging from the baroclinic instability of large-scale background currents saturate at finite amplitudes. However, the evolution of such systems does not stop at this point, as nonlinear interactions between primary eddies frequently lead to the generation of new, and dynamically dissimilar, flow structures. Of particular interest is the tendency of eddies to transfer energy to larger scales of motion through collective instabilities of primary vortices, which is frequently observed in simulations of eddying flows (e.g. Berloff, Kamenkovich & Pedlosky 2009, Kamenkovich, Rypina & Berloff 2015). In such

† Email address for correspondence: tradko@nps.edu

cases, the evolving mesoscale eddy field can generate coherent large-scale eddy-driven patterns (LEDPs). The present paper attempts to identify the key physical mechanisms of LEDP generation and rationalize their spontaneous emergence in certain regions of the parameter space.

A well-known example of LEDPs is provided by quasi-zonal jets which spontaneously form in eddy-rich areas. These jets have been observed in satellite-based observations (Maximenko, Bang & Sasaki 2005; Sokolov & Rintoul 2007), float measurements (Nowlin & Klinck 1986; Orsi, Whitworth & Nowlin 1995) and laboratory experiments (e.g. Matulka & Afanasyev 2015). They populate all ocean basins in high-resolution general circulation models (Nakano & Hasumi 2005; Richards *et al.* 2006; Kamenkovich, Berloff & Pedlosky 2009) and are present in idealized configurations (e.g. Berloff *et al.* 2009; Srinivasan & Young 2012). Numerical simulations suggest that the existence of such jets strongly relies on the action of baroclinic eddies (e.g. Kamenkovich *et al.* 2009, Melnichenko *et al.* 2010). The early models of jet formation (e.g. Held 1975) were based on linear arguments illustrating the interplay between the structure of zonal jets and momentum transport by geostrophic eddies required to maintain mean flows. Several attempts have been made to capture nonlinear dynamics of eddy/mean field interaction. For instance, it has been suggested that locally elevated mixing of potential vorticity (PV) can facilitate further mixing and ultimately produce layered structures described as 'PV staircases' (e.g. Dritschel & McIntyre 2008). The present investigation reveals some alternative generation mechanisms of large-scale jets.

While zonal jets represent perhaps the most spectacular eddy-driven phenomena, LEDPs can also take more irregular and isotropic forms (e.g. Thompson & Young 2006; Kamenkovich *et al.* 2009; Radko, Peixoto de Carvalho & Flanagan 2014). Their spontaneous generation is commonly interpreted as a manifestation of the inverse cascade of energy in two-dimensional turbulence (e.g. Rhines 1994; Larichev & Held 1995; Thompson & Young 2006, 2007). An intriguing aspect of eddy interaction theory concerns the spectrally non-local character of energy transfer. While the classical spectral models (Kraichnan 1967; Kraichnan & Montgomery 1980) envision the sequential coalescence of eddies into larger and larger structures, numerical simulations (Shepherd 1988; Huang & Robinson 1998) suggest the existence of a direct pathway of energy from small to large scales. The interaction between vastly different scales implies that eddies, whose strength is modulated on long wavelengths, can exert a positive feedback on large-scale perturbations. The up-gradient transport of momentum – as well as that of temperature, salinity and isopycnal thickness – has been captured by several numerical studies (Gille & Davis 1999; Nakamura & Chao 2000; Roberts & Marshall 2000). However, despite numerous investigations (Kraichnan 1967; McWilliams & Chow 1981; Chaves & Gama 2000; Cummins & Holloway 2010; among others) specific conditions for anti-diffusive mixing, and the associated dynamics, have not been fully explained.

In this study, the tendency for spontaneous formation of large-scale patterns is illustrated and analysed using a specific example of the two-layer quasi-geostrophic Phillips model of baroclinic instability (Phillips 1951). However, it should be emphasized that our ultimate intent is to introduce a sufficiently broad framework for the analysis of cross-scale interactions, readily adaptable to a wide range of applications. Theoretical progress in this direction can be made by assuming scale separation between distinct components of eddying flows. A particularly promising technique for treating such small-scale/large-scale interactions is multiscale analysis. Multiscale homogenization mechanics, reviewed most recently by Mei & Vernescu

(2010), is an actively developing field with numerous applications in all physical sciences. Typically, multiscale homogenization models assume a periodic primary eddy field and analyse its impact on the evolution of flow components with size exceeding the scale of the background pattern. The multiscale technique is sufficiently generic, making it possible to formulate explicit evolutionary equations for large-scale structures in various physical systems. Importantly, multiscale methods do not assume that developing eddies are small in amplitude. Therefore, they are not limited to the initial stages of eddy growth or to weakly unstable systems (e.g. Pedlosky 1970). Examples of geophysical phenomena explained by multiscale mechanics include the formation of zonal jets in the ocean and atmosphere (Frisch, Legras & Villone 1996; Manfroi & Young 1999, 2002; Legras & Villone 2009; Radko 2011*a*) and the effects of vertical microscale mixing on fine-scale density stratification (Balmforth & Young 2002, 2005; Radko 2011*b*, 2014). Multiscale models formally require asymptotically large-scale separation between the interacting flow components. However, in practice, this condition does not place a particularly stringent constraint on the model applicability. For instance, Radko (2011*c*) examined the effects of limited scale separation through numerical simulations and found that the multiscale model is sufficiently accurate even when the size of large-scale patterns exceeds that of primary eddies by as little as a factor of four.

The simplest primary pattern used in multiscale mechanics is represented by the Kolmogorov model – a parallel shear flow with sinusoidal velocity profile, maintained against viscous dissipation by external forcing (Meshalkin & Sinai 1961; Sivashinsky 1985; Frisch *et al.* 1996; Manfroi & Young 1999, 2002; Balmforth & Young 2002, 2005; Legras & Villone 2009). The major advantage of Kolmogorov-based models is related to their fully analytical tractability. However, questions could be raised as to whether roughly isotropic geophysical eddies, exemplified by ocean rings and weather systems in the atmosphere, can be adequately represented by a parallel flow. Therefore, attempts have been made to move beyond the Kolmogorov model by assuming two-dimensional – cellular, hexagonal or dipolar – primary patterns (e.g. Gama, Vergassola & Frisch 1994; Novikov & Papanicolau 2001; Radko 2011*a*,*c*), including translating structures (Cushman-Roisin, McLaughlin & Papanicolaou 1984; Connaughton *et al.* 2010). However, despite the appealing generality and physical transparency of multiscale methods, their utility has been mostly qualitative and conceptual. The major obstacle for even wider and more quantitative application of multiscale methods is their strong sensitivity to the background eddy patterns. For instance, not only the magnitude but even the sign of the effective viscosity predicted by multiscale models depends on the assumed small-scale eddy model (e.g. Gama *et al.* 1994; Novikov & Papanicolau 2001; Radko 2011*a*,*c*). This ambiguity implies that the successful application of multiscale methods is contingent on the proper choice of the background pattern.

One of the key objectives of this paper is to demonstrate that the aforementioned limitations may not arise when multiscale solutions are based on dynamically consistent eddy models, rather than on highly idealized analytical patterns. Such solutions are directly applicable to – and testable by – observations and numerical simulations. To the best of our knowledge, representative eddy patterns have not been employed yet in the extant geophysical multiscale models, and this possibility is explored in the present paper. The proposed average eddy (AE) model, in which the background pattern is taken from numerical simulations, retains the dynamic transparency of the conventional multiscale theories. At the same time, it brings in much improved relevance and accuracy, as illustrated here on the example of

baroclinic instability in the Phillips framework. Using the multiscale AE model, we evaluate effective eddy viscosity, validate the model using direct numerical simulations, identify the essential dynamics of the up-gradient momentum transport and analyse conditions for the spontaneous generation of large-scale flows.

The paper is organized as follows. In §2, we present a series of preliminary simulations which demonstrate the tendency for the spontaneous emergence of LEDPs. We emphasize the sensitivity of this phenomenon to governing parameters and demonstrate the significance of the spectrally non-local interactions for the growth of unstable LEDPs. In §3, the generation of LEDPs is treated as a multiscale problem, which is then used to evaluate the effective eddy viscosity of large-scale zonal currents (§4). We identify the dominant balances revealed by multiscale expansion and interpret the origin of LEDPs in the Phillips model (§5). In §6, we discuss conditions that favour spontaneous formation of LEDPs. We summarize our findings and draw conclusions in §7.

2. Preliminary simulations

Consider a baroclinically unstable zonal flow represented by the two-layer quasi-geostrophic model (e.g. Pedlosky 1987)

$$
\left.\begin{aligned}
\frac{\partial Q_1}{\partial t} + J(\Psi_1, Q_1) &= \nu \nabla^4 \Psi_1, \quad Q_1 = \nabla^2 \Psi_1 + \frac{f^2}{g'H_1}(\Psi_2 - \Psi_1) + \beta y, \\
\frac{\partial Q_2}{\partial t} + J(\Psi_2, Q_2) &= \nu \nabla^4 \Psi_2 - \gamma \nabla^2 \Psi_2, \quad Q_2 = \nabla^2 \Psi_2 + \frac{f^2}{g'H_2}(\Psi_1 - \Psi_2) + \beta y,
\end{aligned}\right\} \quad (2.1)
$$

where (Ψ_1, Ψ_2) are the streamfunctions, (Q_1, Q_2) are the potential vorticities and (H_1, H_2) are the depths of the upper and lower layers respectively; $g' = (\Delta\rho/\rho)g$ is the reduced gravity, ρ is the density, f is the Coriolis parameter, $\beta = (\partial f/\partial y)$, ν is the lateral viscosity and γ is the bottom drag coefficient. The flow field (Ψ_1, Ψ_2) is separated into the Phillips basic state $(\bar{\bar{\psi}}_1, \bar{\bar{\psi}}_2)$, representing the laterally homogeneous zonal current, and the perturbation (ψ_1, ψ_2). Without loss of generality, we consider a basic state in which the lower layer is motionless $(\bar{\bar{\psi}}_2 = 0)$ and express the governing equations (2.1) in terms of (ψ_1, ψ_2).

To reduce the number of governing parameters, the system is non-dimensionalized using R_{d1}, $|U|$ and $R_{d1}/|U|$ as the scales of length, velocity and time respectively; U is the basic velocity of the upper layer and $R_{d1} = \sqrt{g'H_1}/f$ is the radius of deformation of the upper layer. The resulting non-dimensional system takes the form

$$
\left.\begin{aligned}
\frac{\partial q_1}{\partial t} + J(\psi_1, q_1) + (\beta_{nd} + s)\frac{\partial \psi_1}{\partial x} + s\frac{\partial q_1}{\partial x} &= \nu_{nd}\nabla^4 \psi_1, \quad q_1 = \nabla^2 \psi_1 + (\psi_2 - \psi_1), \\
\frac{\partial q_2}{\partial t} + J(\psi_2, q_2) + (\beta_{nd} - sr)\frac{\partial \psi_2}{\partial x} &= \nu_{nd}\nabla^4 \psi_2 - \gamma_{nd}\nabla^2 \psi_2, \quad q_2 = \nabla^2 \psi_2 + r(\psi_1 - \psi_2),
\end{aligned}\right\} \quad (2.2)
$$

where $\beta_{nd} = (\beta R_{d1}^2)/|U|$, $\nu_{nd} = \nu/(R_{d1}|U|)$, $\gamma_{nd} = (\gamma R_{d1})/|U|$, $r = (H_1/H_2)$ are the key non-dimensional parameters, $s = U/|U|$ is the sign of the background velocity and (q_1, q_2) are the perturbation PV fields. Thus, in non-dimensional units, the Phillips basic state is $\bar{\bar{u}}_{1,2} = -(\partial\bar{\bar{\psi}}_{1,2}/\partial y) = (s, 0) = (\pm 1, 0)$.

In the following numerical experiments, we shall assume doubly periodic boundary conditions for (ψ_1, ψ_2) in x and y, and integrate the governing system (2.2) using the dealiased pseudospectral model employed in Radko *et al.* (2014). Figure 1(*a,c,e*)
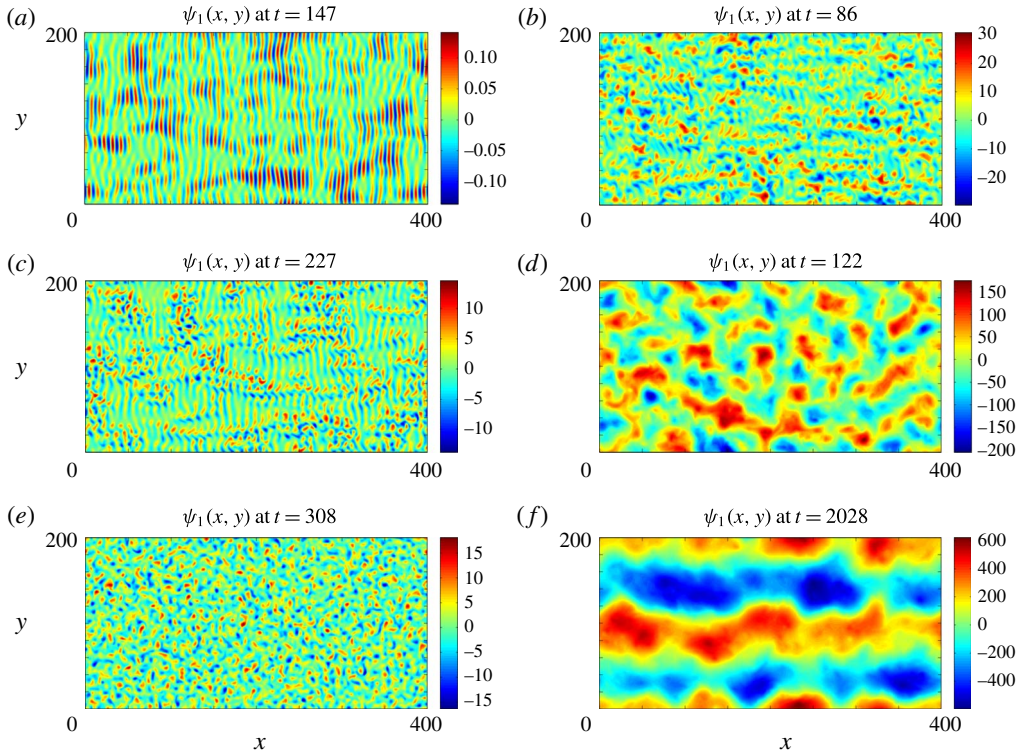
FIGURE 1. (Colour online) Typical instantaneous patterns of the upper-layer stream-function at various evolutionary stages. (*a,c,e*) The flow evolution in the high-drag experiment ($\gamma_{nd} = 0.5$). The corresponding low-drag simulation ($\gamma_{nd} = 0.05$) is shown in (*b,d,f*). The other governing parameters are identical: $(\beta_{nd}, r, \nu_{nd}, s) = (0.1, 1/3, 0.05, 1)$ and $(L_x, L_y) = (400, 200)$. The reduction of the bottom drag coefficient results in the spontaneous generation of large-scale patterns.

presents a typical simulation in the baroclinically unstable regime. For this experiment, we have used

$$(\beta_{nd}, r, \gamma_{nd}, \nu_{nd}, s) = (0.1, 13, 0.5, 0.05, 1). \tag{2.3}$$

In dimensional units, these parameters describe, for instance, an eastward basic current with $U = 0.05$ m s^{-1}, $\beta = 10^{-11}$ m^{-1} s^{-1}, $H_1 = 1$ km, $H_2 = 3$ km, $\gamma = 10^{-6}$ s^{-1}, $\nu = 60$ m^2 s^{-1} and $R_{d1} = 25$ km – scales that are representative of typical mid-ocean flows. The size of the computational domain in figure 1(*a,c,e*) is $(L_x, L_y) = (400, 200)$, which is equivalent to $10\,000$ km $\times$ 5000 km, and it is resolved by a uniform mesh with $N_x \times N_y = 768 \times 384$ elements. The simulation was initialized from rest by a small-amplitude random computer-generated (ψ_1, ψ_2) distribution. The active statistically steady eddying motion driven by baroclinic instability was established after a few growth rate periods. Figure 1(*a*) shows a typical instantaneous ($t = 147$) streamfunction field (ψ_1) in the initial stage of linear growth. As expected from linear stability theory, the most rapidly growing perturbations take the form of meridional harmonics. Figure 1(*c*) ($t = 227$) presents the second evolutionary stage – development of secondary instabilities, which act to distort the primary modes, adversely affecting their growth. Finally, by $t = 308$, figure 1(*e*), the system enters the quasi-equilibrium

stage, characterized by irregular transient mesoscale patterns. The simulation was extended further in time (to $t = 3000$), but no additional qualitative changes were observed.

A substantially different pattern emerged in the simulation shown in figure 1(*b,d,f*). This experiment is identical to that in figure 1(*a,c,e*) in all respects except for the bottom drag coefficient, which was reduced by an order of magnitude to $\gamma_{nd} = 0.05$. While the initial stages of both simulations are similar, the long-term evolution of the low-drag experiment (figure 1*f*) is characterized by the emergence of large-scale zonally elongated patterns. They gradually intensify and ultimately evolve into quasi-steady and largely barotropic structures dominating the final streamfunction field. The dramatically different outcomes of the experiments in figures 1(*e*) and 1(*f*) suggest that the spontaneous generation of LEDPs is controlled by the competition between the destabilizing action of mesoscale eddies and the damping tendency of bottom drag.

Since this study is focused on cross-scale interactions, it becomes necessary at this point to introduce a specific and convenient operational definition of a 'large-scale' pattern. In the following analysis, we assume that LEDPs consist of Fourier harmonics with wavelengths exceeding the cutoff scale L_{cr}. This critical scale is set to $L_{cr} = 20$ and this convention will be used consistently throughout our study. For instance, to further isolate the role of multiscale interactions in LEDP generation, we present a 'filtered' simulation (figure 2) in which all Fourier components with meridional wavelengths exceeding $L_{cr} = 20$ are reset to zero at each time step, except for the fundamental meridional harmonic

$$\psi_{1,2} = \text{Re} \left[A_{1,2} \exp \left(\text{i} \frac{2\pi}{L_y} y \right) \right]. \tag{2.4}$$

Such a wide spectral gap precludes the possibility of LEDP generation through the sequential coalescence of eddies into larger and larger structures, associated with the upscale energy cascade in predominantly two-dimensional turbulence. Additionally, the bottom drag in this experiment is applied to mesoscale components but not to the large-scale mode (2.4). Neglecting the large-scale bottom drag ($\gamma_{ls} = 0$) but retaining the substantial drag on mesoscale components ($\gamma_{ms} = 0.5$) allows us to isolate and quantify the impact of eddies on the large-scale current. The filtered simulation (figure 2) is characterized by the monotonic growth of (2.4) – the only large-scale mode present. The mode (2.4) represents the zonal flow and therefore it is baroclinically stable (recall that the basic Phillips flow is also zonal). Thus, its amplification is entirely due to the action of eddies. Since the cascade is precluded, the conclusion that one might draw from this experiment is that spectrally non-local interactions are sufficiently vigorous and efficient to induce the spontaneous generation of LEDPs. The evolutionary time scales and the resulting flow patterns in figure 2 are similar to those realized in its unfiltered counterpart (figure 1*b,d,f*), in which bottom drag is uniformly low at all scales ($\gamma_{nd} = 0.05$).

Figure 3(*a*) presents the time record of the upper-layer amplitude ($|A_1|$) of the large-scale harmonic (2.4) as a function of time for the experiment in figure 2. The amplitude is plotted in logarithmic coordinates, and therefore the straight segment of the curve in figure 2 at moderate values of $|A_1|$ is indicative of the exponential growth of the perturbation. This, in turn, suggests that the emergence of the LEDP in this simulation can be interpreted as a form of instability driven by interactions between the large-scale harmonic and the mesoscale eddy field. To be more specific, one might argue that the acceleration of the large-scale current (figure 2*a,c,e*) is a manifestation
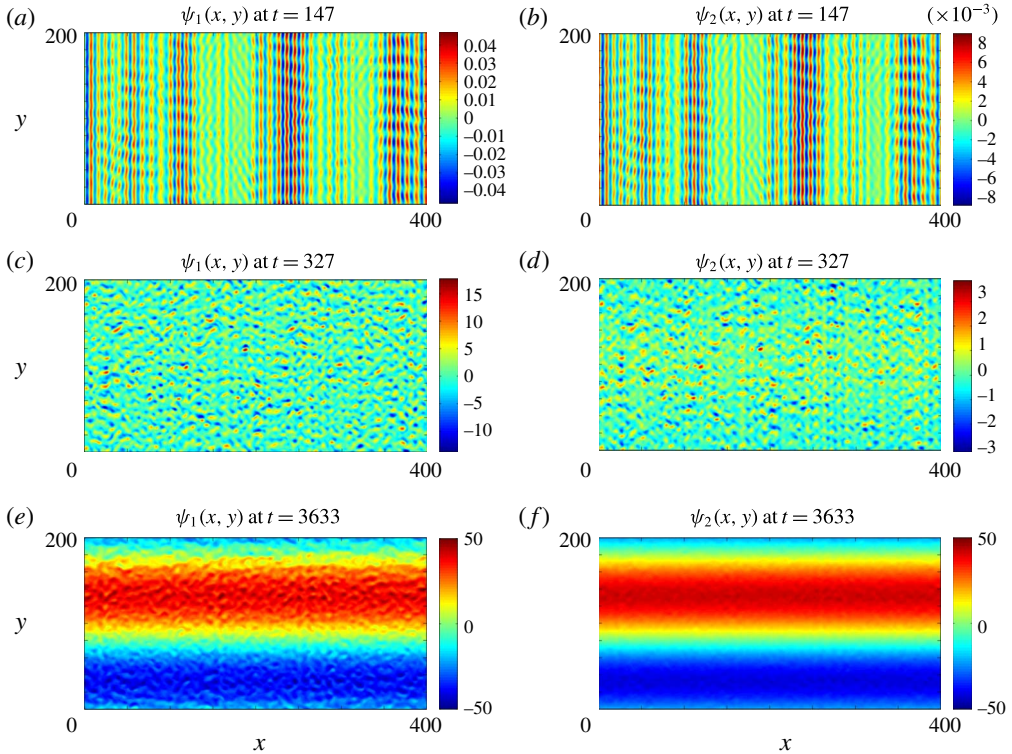
FIGURE 2. (Colour online) The filtered simulation in which all Fourier components with meridional wavelengths exceeding $L_{cr} = 20$ are reset to zero at each time step, except for the fundamental meridional harmonic (2.4). The upper- and lower-layer streamfunctions are shown in (a,c,e) and (b,d,f) respectively. The fundamental harmonic grows in time, eventually dominating the flow field, which reflects the destabilizing nature of mesoscale variability.

of the negative eddy viscosity phenomenon (Starr 1968). This suggestion is also supported by the observation that the growth rate of the large-scale perturbation is proportional to its wavenumber ($m = 2\pi/L_y$) squared, as expected for the linear diffusion equation with negative diffusivity.

Figure 3(b) presents a series of simulations which are identical to that in figure 2 in all respects except for the meridional extent of the domain (L_y) – the latter is systematically varied from $L_y = 100$ to $L_y = 1600$. The growth rate (λ) of the fundamental mode (2.4) is then diagnosed from numerics and plotted as a function of the large-scale wavenumber m in logarithmic coordinates. The data points (figure 3b) align along the straight line with slope corresponding to the power law $\lambda \propto m^2$. The effective eddy viscosity associated with this amplification is $K = -1.2$. It is interesting that if the spectral gap is not enforced in the simulation, while the direct influence of bottom drag on the large-scale mode (2.4) is still excluded ($\gamma_{ls} = 0$), the effective viscosity reduces to $K = -0.9$. The limited sensitivity ($\sim 25\%$) of eddy viscosity to the presence/absence of intermediate scales ($L_{cr} < L < L_y$) is suggestive. It offers yet another indication that, in the parameter regime explored here, the evolution of large-scale patterns is controlled by spectrally non-local processes.
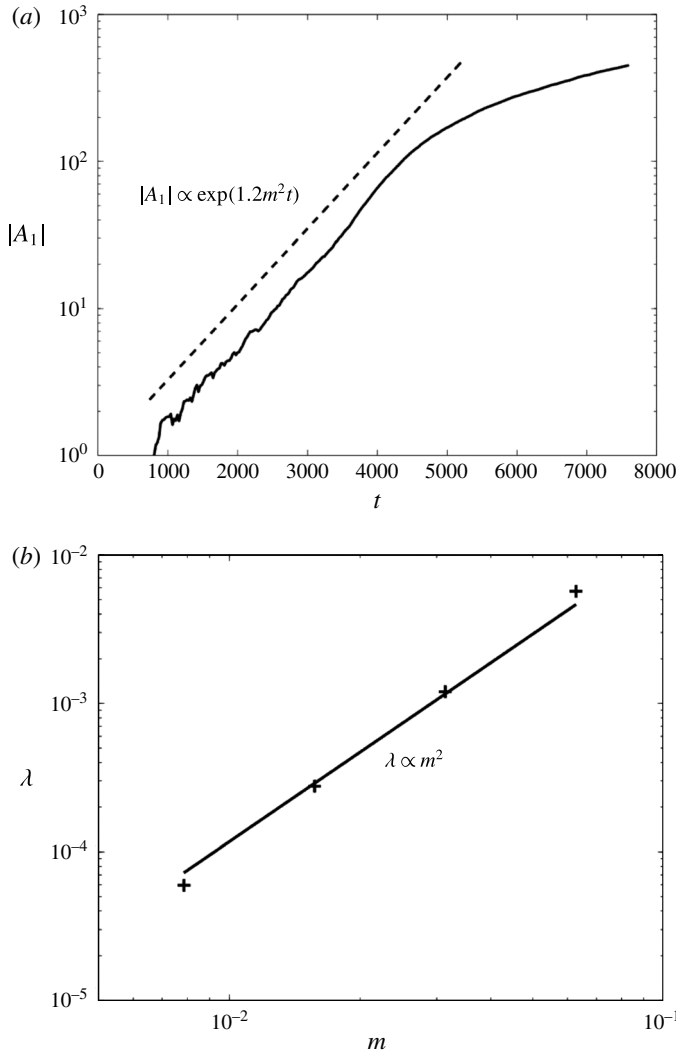
FIGURE 3. (*a*) The amplitude of the fundamental harmonic (2.4) is plotted on a logarithmic scale as a function of time (solid curve) for the filtered calculation in figure 2. The relatively straight segment between $t = 1000$ and $t = 4000$ corresponds to exponential amplification, which, in turn, suggests linear instability of the large-scale mode (2.4). The straight dashed line represents the amplification corresponding to the uniform negative viscosity of $K = -1.2$. (*b*) The growth rate of the large-scale perturbation is plotted as a function of its wavenumber (m) in logarithmic coordinates. The numerical results are indicated by the plus signs and the straight line corresponds to the anti-diffusive scaling $\lambda \propto m^2$.

While the influence of eddies on large-scale perturbations is destabilizing, leading to the amplification of large-scale patterns, bottom drag and beta-effect act in the opposite sense. Figure 4 combines a series of simulations performed with various values of $(s, \beta_{nd}, \gamma_{nd})$. The bottom drag in these experiments is spatially uniform at all scales and spectral filtering is not applied. For each simulation, we quantify the
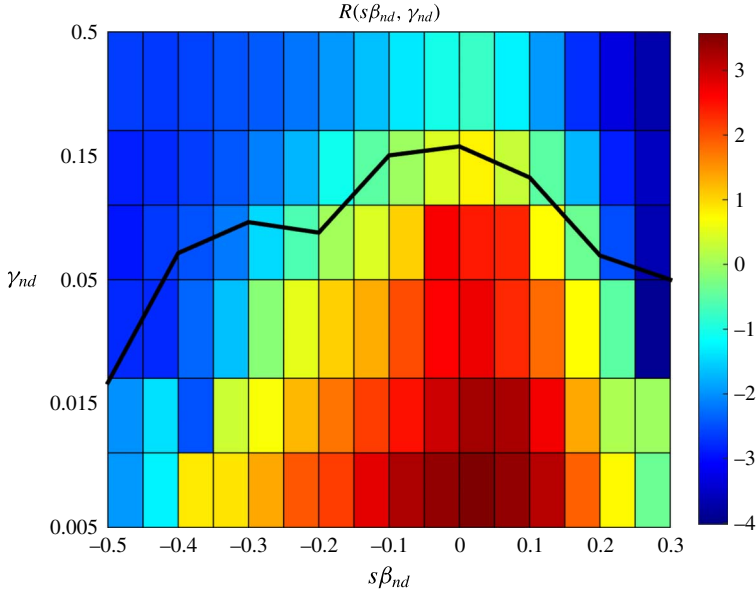
FIGURE 4. (Colour online) The discriminator variable (R) defined in (2.5) is plotted as a function of $s\beta_{nd}$ and γ_{nd}. The positive values of R (shown in red) represent the LEDP-dominated simulations and the negative R (shown in blue) reflect the predominantly mesoscale dynamics. The logarithmic (linear) axis is used for γ_{nd} ($s\beta_{nd}$). The heavy solid curve represents the theoretical estimate (§ 6) of the boundary between the LEDP-dominated and mesoscale-dominated regimes.

relative magnitude of mesoscale eddies and LEDPs using the discriminator variable

$$R = \ln\left(\frac{E_{LEDP}}{E_{MS}}\right), \tag{2.5}$$

where E_{MS} and E_{LEDP} represent the perturbation energy contained in the mesoscale and large-scale eddy fields respectively. The mean perturbation energy of the two-layer system is

$$E = \left\langle \frac{r}{2(1+r)}\,|\nabla\psi_1|^2 + \frac{1}{2(1+r)}\,|\nabla\psi_2|^2 + \frac{r}{2(1+r)}(\psi_2 - \psi_1)^2 \right\rangle, \tag{2.6}$$

where the angled brackets represent averaging in (x, y). The mesoscale (large-scale) components are represented by a superposition of Fourier harmonics with the wavelengths $L < L_{cr} = 20$ ($L > L_{cr}$). The discriminator R, diagnosed at the end of each simulation ($t = 2000$), is plotted as a function of $s\beta_{nd}$ and γ_{nd} in figure 4. For each value of (s, β_{nd}), the fraction of energy contained in large scales monotonically increases with decreasing γ_{nd}, and the system eventually transitions to the LEDP-dominated regime. For given γ_{nd}, LEDPs are more likely to emerge at low values of β_{nd}.

The results presented in this section are generally consistent with the conventional views on the dynamics of mesoscale turbulence (Rhines 1977; Larichev & Held 1995; Thompson & Young 2006, 2007). For instance, the link between weak bottom

drag and spontaneous generation of large-scale structures has been noted in several studies (Nadiga 2006; Nadiga & Straub 2010; Radko *et al.* 2014). The upscale barotropic cascade is known to be suppressed by large bottom drag as well as by large beta (e.g. Held & Larichev 1996; Thompson & Young 2006, 2007; Berloff *et al.* 2011). These effects may be invoked to broadly rationalize salient features of the presented experiments: (i) the limited amplitude of large-scale components and (ii) the dominance of spectrally non-local interactions when the bottom drag is substantial. The following model attempts to explain the eddy/mean-flow interaction on a more quantitative and mechanistic level (§§ 3–5). We shall focus on the moderately high-drag regime, which is readily amenable to multiscale treatment, and attempt to explain the transition to LEDP-favourable conditions in certain regions of the $(s\beta_{nd}, \gamma_{nd})$ parameter space (§ 6).

3. Generation of LEDPs as a multiscale problem

In this section, the problem of spontaneous generation of LEDPs is treated using techniques of asymptotic multiscale analysis (Kevorkian & Cole 1996; Mei & Vernescu 2010). Details are relegated to the Appendix, and here we summarize the key steps. The interaction between vastly dissimilar flow components is described using new temporal and spatial variables (T, Y) over which the background eddy pattern is modulated:

$$Y = \varepsilon y, \quad T = \varepsilon^2 t, \quad (3.1a,b)$$

where $\varepsilon \ll 1$ is a measure of the relative spatial scales of the background eddies and large-scale flow. We are concerned by the ability of small-scale eddies, represented by the streamfunction fields $\bar{\psi}_{1,2}(x, y, t)$, to affect the slow evolution of a broad zonal current. The primary eddy field is assumed to be fully developed and statistically homogeneous on large scales. In terms of magnitude, it represents the dominant temporally variable component, and $\bar{\psi}_{1,2} \sim O(1)$ in the expansion. Thus, the strength of primary eddies is comparable to the Phillips basic flow $\bar{\bar{u}}_{1,2} = (\pm 1, 0)$ that generates them, and therefore the eddy dynamics are fundamentally nonlinear.

We now examine how this large-amplitude small-scale eddy field interacts with the large-scale zonal perturbation. The latter is taken to be barotropic at the leading order, which is consistent with our preliminary simulations (figure 2) and can be rationalized theoretically (see the Appendix):

$$\psi_{1,2}^{(0)} = \psi^{(0)}(Y, T). \quad (3.2)$$

Since the zonal jet (3.2) varies on large scales, its velocity is weak, $u^{(0)} = -\varepsilon \psi_Y^{(0)}$, and the shear induced by the jet is even weaker, $sh^{(0)} = \varepsilon^2 \psi_{YY}^{(0)}$. Both displacement and shear induced by the large-scale jet perturb and modulate the background eddy field $\bar{\psi}_{1,2}$. These dynamics are reflected by expressing the total streamfunction field $(\psi_{1,2})$ as follows:

$$\begin{aligned}
\psi_{1,2} &= \psi^{(0)}(Y, T) + \bar{\psi}_{1,2}(x, y, t) + \varepsilon \psi_Y^{(0)}(Y, T) \cdot \tilde{\psi}_{1,2}^{(1)}(x, y, t) \\
&\quad + \varepsilon^2 \psi_{YY}^{(0)}(Y, T) \cdot \tilde{\psi}_{1,2}^{(2)}(x, y, t) + O(\varepsilon^3).
\end{aligned} \quad (3.3)$$

Equation (3.3) can be readily obtained (see the Appendix) using a formal expansion of $\psi_{1,2}$ in powers of ε. As is common to all modulational stability analyses, the perturbation components $(\psi_{1,2}^{(1)}, \psi_{1,2}^{(2)})$ in (3.3) are expressed as products of

modulating functions $(\psi_Y^{(0)}, \psi_{YY}^{(0)})$, which vary on large spatial/temporal scales, and the corresponding auxiliary functions $(\tilde{\psi}_{1,2}^{(1)}, \tilde{\psi}_{1,2}^{(2)})$, varying on small scales:

$$\psi_{1,2}^{(1)} = \psi_Y^{(0)}(Y, T) \cdot \tilde{\psi}_{1,2}^{(1)}(x, y, t), \quad \psi_{1,2}^{(2)} = \psi_{YY}^{(0)}(Y, T) \cdot \tilde{\psi}_{1,2}^{(2)}(x, y, t). \quad (3.4a,b)$$

The auxiliary functions $(\tilde{\psi}_{1,2}^{(1)}, \tilde{\psi}_{1,2}^{(2)})$ are related to the background pattern $\bar{\psi}_{1,2}$ by a set of partial differential equations (A 6), (A 9) and (A 10) in small-scale variables (x, y, t). Determining $\tilde{\psi}_{1,2}^{(1)}$ and $\tilde{\psi}_{1,2}^{(2)}$ for given $\bar{\psi}_{1,2}$ – the background small-scale eddy field – is referred to as solving the first and second auxiliary problems respectively.

   The large-scale modulation of the eddy field in (3.4) is essential for triggering feedbacks of eddies on large-scale jets. The interaction of the jet (represented by the first term on the right-hand side of (3.3)) with the background eddy field (the second term in (3.3)) generates the modulated perturbations (terms three and four). These perturbations $(\psi_{1,2}^{(1)}, \psi_{1,2}^{(2)})$, in turn, interact with the basic field $\bar{\psi}_{1,2}$, which modifies the large-scale pattern $\psi^{(0)}$. The system evolution resulting from the interplay between the large-scale current and modulated eddy perturbations is represented by the diffusion equation

$$\frac{\partial}{\partial T} u^{(0)} = K \frac{\partial^2}{\partial Y^2} u^{(0)}, \quad (3.5)$$

where K is the effective eddy viscosity (see the Appendix). For the sake of simplicity, in the present formulation we have linearized all asymptotic equations with respect to $\psi^{(0)}$ terms. However, it should be emphasized that multiscale models can incorporate the nonlinearities in the evolutionary large-scale equations in a rather straightforward manner (e.g. Gama *et al.* 1994; Novikov & Papanicolau 2001).

   In view of (3.1), it is apparent that (3.5) retains its form even when it is written using the original (small-scale) temporal and spatial variables (t, y). The multiscale model makes it possible to express K in terms of the primary eddy field $\bar{\psi}_{1,2}$ and the auxiliary functions $(\tilde{\psi}_{1,2}^{(1)}, \tilde{\psi}_{1,2}^{(2)})$:

$$K = -\frac{1}{1+r} \left[\left\langle r \frac{\partial \bar{\psi}_1}{\partial x} \left(2 \frac{\partial \tilde{\psi}_1^{(2)}}{\partial y} + \tilde{\psi}_1^{(1)} \right) + \frac{\partial \bar{\psi}_2}{\partial x} \left(2 \frac{\partial \tilde{\psi}_2^{(2)}}{\partial y} + \tilde{\psi}_2^{(1)} \right) \right\rangle \right], \quad (3.6)$$

where angled brackets represent averaging in (x, y) and square brackets represent averaging in t. The instantaneous counterpart of (3.6), in which averages are taken in space only, will be denoted by $K_{inst}(t)$:

$$K_{inst} = -\frac{1}{1+r} \left\langle r \frac{\partial \bar{\psi}_1}{\partial x} \left(2 \frac{\partial \tilde{\psi}_1^{(2)}}{\partial y} + \tilde{\psi}_1^{(1)} \right) + \frac{\partial \bar{\psi}_2}{\partial x} \left(2 \frac{\partial \tilde{\psi}_2^{(2)}}{\partial y} + \tilde{\psi}_2^{(1)} \right) \right\rangle. \quad (3.7)$$

   It is interesting and perhaps somewhat counterintuitive that while the displacement-induced and shear-induced effects appear at different orders in the streamfunction series (3.3), both processes are represented at the leading order in the expression for eddy viscosity (3.6). The sign of K determines whether eddies exert positive or negative feedback on large-scale patterns. If $K < 0$, we can expect eddy-induced amplification of large-scale patterns, but $K > 0$ would imply that eddies act to suppress them.

   One of the complications that commonly arises in multiscale modelling is that the interaction of primary eddies with large-scale flows may not be the only

mechanism producing the perturbation fields $(\psi_{1,2}^{(1)}, \psi_{1,2}^{(2)})$. An alternative source of these perturbations is small-scale instability. This possibility is particularly relevant for the baroclinically unstable flows considered in our study. The irregular and time-dependent mesoscale variability at high Reynolds numbers is inherently susceptible to various secondary instabilities. These small-scale instabilities, by themselves, may not systematically affect large-scale patterns. Nevertheless, their presence complicates the analysis of the solutions obtained, since the unstable modes amplify in time and can eventually mask the processes of interest – the generation of perturbations through the interaction of the primary eddy field $\bar{\psi}_{1,2}$ with the large-scale flow $\psi^{(0)}$ and the feedback of these perturbations on the large-scale current. The majority of classical multiscale models deal with this complication either by restricting analysis to sufficiently low Reynolds numbers required to suppress the secondary small-scale instabilities (Meshalkin & Sinai 1961; Nepomnyashchy 1976; Sivashinsky 1985; Frisch, She & Sulem 1987; Gama *et al.* 1994; Wirth, Gama & Frisch 1995; among many others) or by *a priori* ignoring the fast time variation of small-scale components (e.g. Novikov & Papanicolau 2001; Radko 2014). Both approaches are legitimate, as a starting point, and could be easily applied to our problem. However, this study provides us with the opportunity to develop an alternative non-invasive multiscale method, resulting in a more realistic description of eddy/LEDP interactions, which we describe next.

4. The AE model

Modulational stability analysis constitutes an effective analytical technique, commonly used to elucidate the dynamics of cross-scale interactions in most physical sciences (e.g. Mei & Vernescu 2010). Perhaps the biggest obstacle for even wider application of multiscale models is the high sensitivity of model predictions to the assumed eddy structure, which severely limits the practical value of an otherwise very promising technique. The approach advocated in this study may offer a simple and effective remedy for the problem. Instead of focusing on idealized backgrounds (e.g. harmonic, hexagonal or dipolar) we propose to consider more realistic and dynamically consistent patterns that could be readily obtained from simulations. In the following examples, the primary eddy pattern $\bar{\psi}_{1,2}(x, y, t)$ is obtained by integrating the governing equations (2.2) subject to doubly periodic boundary conditions in (x, y). These calculations are accompanied by the integrations of auxiliary problems (A 9) and (A 10), making it possible to obtain $(\tilde{\psi}_{1,2}^{(1)}, \tilde{\psi}_{1,2}^{(2)})$ and, ultimately, the eddy viscosity (3.6). Experimentation with various computational domains indicated that the results are not particularly sensitive to the size as long as it significantly exceeds the typical eddy scale. Multiscale models tend to be slightly more accurate when the meridional domain size is increased, and therefore the solutions presented here were obtained using relatively large areas $(L_x, L_y) = (80, 320)$.

Figure 5 shows typical fully developed streamfunction patterns of the primary eddy field and the corresponding auxiliary functions, obtained as follows. First, the governing equations (2.2) were integrated in time starting from a small-amplitude random perturbation for $\bar{\psi}_{1,2}$. The model parameters for the experiment in figure 5 are the same as in figure 1(*a,c,e*), and are listed in (2.3). It should be recalled that these parameters correspond to stable large-scale perturbations (figure 1*a,c,e*) if bottom drag is assumed to be uniform at all scales ($\gamma_{ms} = \gamma_{ls} = \gamma_{nd}$) and to the amplification of large-scale modes (figures 2 and 3) if direct effects of drag on large scales are ignored ($\gamma_{ms} = \gamma_{nd}, \gamma_{ls} = 0$). By $t_{00} = 300$, the system evolved to
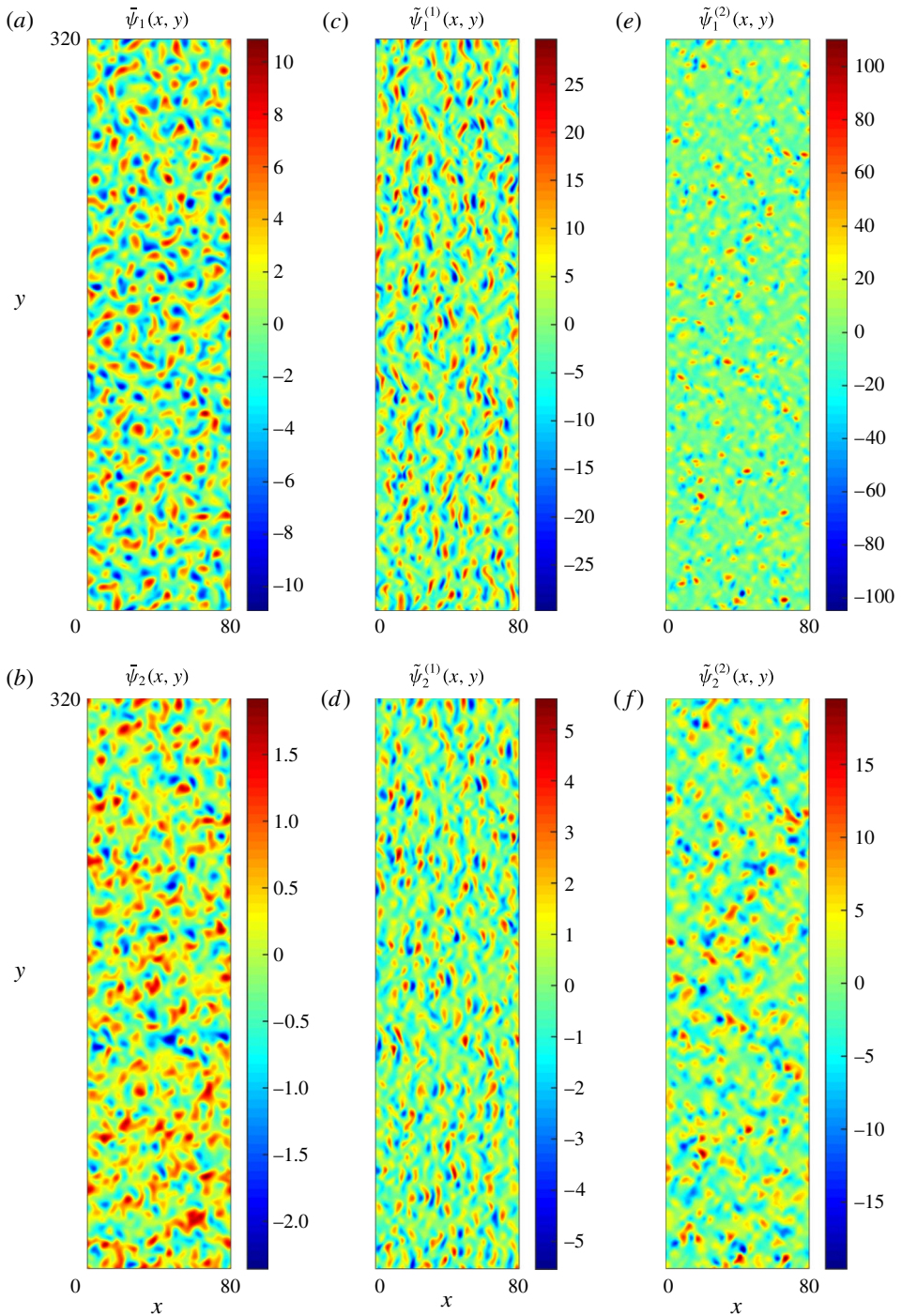
FIGURE 5. (Colour online) Typical upper/lower streamfunction patterns $\bar{\psi}_{1,2}$ (a,b) along with the corresponding solutions of the first (c,d) and second (e,f) auxiliary problems.

the statistically steady quasi-equilibrium state. The experiment was then extended by $\Delta t = 5$ and, during this interval, it was accompanied by concurrent integration of the auxiliary problems (A 9) and (A 10) starting from $\tilde{\psi}_{1,2}^{(1,2)}(t_{00}) = 0$. Figure 5(a,b) presents the primary eddy fields $\bar{\psi}_{1,2}$ at $t = t_{00} + \Delta t$, and the corresponding solutions of the first and second auxiliary problems are shown in figures 5(c,d) and 5(e,f) respectively. During the period $t_{00} < t < t_{00} + \Delta t$, the eddy viscosity (3.7) gradually decreased from zero to $K_{inst} = -0.69$, indicating that the eddy transfer of momentum occurred in the up-gradient sense.

Extensions of the auxiliary integrations for much longer periods of time, however, revealed a serious complication: the unbounded growth of the auxiliary functions ($\tilde{\psi}_{1,2}^{(1,2)}$), caused by the instability of the linear operator A in (A 6). As discussed earlier (§ 3), the appearance of new small-scale instabilities in the irregular and time-dependent eddying flows is natural and expected. The auxiliary problems (A 9) and (A 10) are structurally similar to the system (2.2) that governs the evolution of background eddies, and therefore they are subject to similar (baroclinic) instabilities. The interaction of the auxiliary functions with the background eddy field – the interaction represented by the Jacobian terms in A – tends to intensify rather than suppress these instabilities. Unless this issue is addressed, the indefinite growth of the auxiliary functions can limit the utility of the multiscale model.

The crux of the proposed approach is a simple observation that even when operator A is unstable, the asymptotic solution (3.3) still remains valid and accurate for relatively long periods of time. If λ_A represents the largest growth rate of A, then the expansion leading to (A 9) and (A 10) fails (in the worst-case scenario) only after a period of $t_f \sim (1/\lambda_A) \ln(\varepsilon^{-1}) \gg 1$. The time of adjustment of the eddy field to the large-scale forcing, on the other hand, is an order-one quantity: $t_{adj} = O(1)$ – the time scale set by a typical eddy turnaround period. The asymptotic disparity of the scales of adjustment and of the model failure ($t_{adj} \ll t_f$) justifies the use of the multiscale framework for calculating – and physically explaining the selection of – the effective eddy viscosity.

The technical problem that arises at this point is that the amplification of auxiliary functions in time makes it difficult to accurately evaluate the time-mean values of K in (3.6) from a single experiment. This complication, however, is readily resolved by ensemble averaging of the results over a large number (N) of realizations. For a given set of parameters, the auxiliary problems were repeatedly integrated over time intervals $[t_0, t_0 + \Delta T]$ greatly exceeding the eddy adjustment time scale ($\Delta T \gg t_{adj}$), where $t_0 = t_{00} + n\Delta T$, $n = 1, \ldots, N$. The initial conditions for each integration of auxiliary problems were taken to be $\tilde{\psi}_{1,2}^{(1,2)}(t_0) = 0$. Then, the N time records of $K_{inst}(\tau)$, where $\tau = t - t_0$, obtained at each integration were averaged over all realizations, which effectively isolated the dynamically significant signal.

Figure 6 presents the ensemble-averaged time record of eddy viscosity $K_{inst}(\tau)$ for $N = 445\,000$ and $\Delta T = 25$. As expected, the evolution of $K_{inst}(\tau)$ is a two-stage process. First, it gradually decreases from zero to its preferred equilibrium value ($1 < \tau < 5$) and subsequently remains largely uniform ($\tau > 5$). The mean value evaluated for the second stage is interpreted as the eddy viscosity suggested by the multiscale model. While the ensemble-averaged $K_{inst}(\tau)$ converges with increasing τ to a well-defined equilibrium level, the individual realizations are characterized by irregular amplifying oscillations about this mean value.

In order to assess the accuracy of the multiscale model, the effective eddy viscosity was also diagnosed numerically. For this, we integrated the governing equations (2.2) using the version of the spectral code (cf. § 2) in which the bottom drag operator was
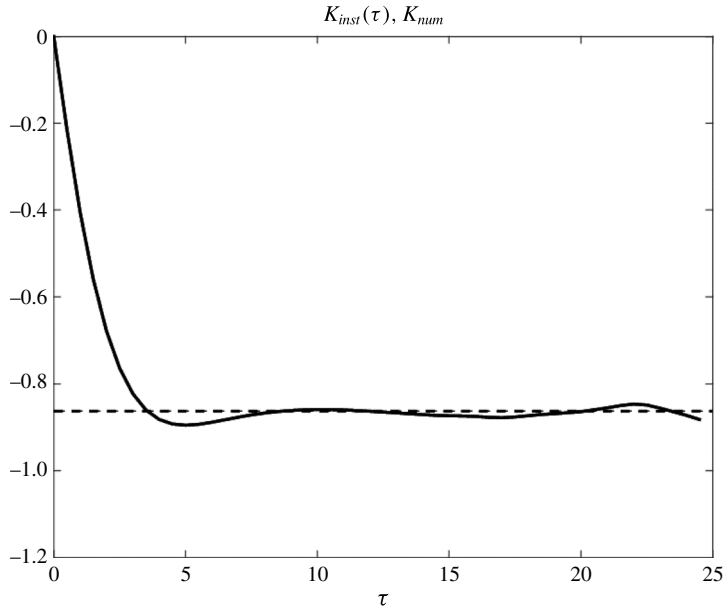
FIGURE 6. The ensemble-averaged eddy viscosity as a function of time. After the initial period of adjustment ($\tau < 5$), the instantaneous eddy viscosity K_{inst} obtained with the multiscale model (indicated by the solid curve) becomes largely uniform and closely matches the corresponding numerical estimate, represented by the dashed horizontal line.

applied to all spectral modes except for the fundamental harmonic (2.4). As a result, this mode amplified exponentially due to the action of eddies. The growth rate (λ) realized in this simulation was then used to infer the eddy viscosity $K_{num} = -\lambda/m^2$, where $m = 2\pi/L_y$ is the fundamental wavenumber. The numerical estimate of eddy viscosity is indicated in figure 6 by the horizontal dashed line. The close agreement between the numerical and theoretical estimates leaves no doubt that the formalism of multiscale modelling can be successfully applied to realistic and dynamically consistent eddy patterns.

To explore the parameter space, we performed a series of simulations analogous to that in figure 6 for a range of $s\beta_{nd}$ and compared (figure 7) the multiscale results with the corresponding numerical estimates of eddy viscosity. Figure 7 indicates that the multiscale model not only correctly produces the negative sign and typical magnitude of eddy viscosity but also accurately captures the variation of K with $s\beta_{nd}$. The pattern of $K(s\beta_{nd})$ is of interest in its own right. While the intensity of eddies, as measured for instance by the root mean square perturbation velocity, tends to be significantly higher for the westward propagating basic current ($s = -1$), the eddy viscosity pattern is reversed. The largest values of eddy viscosity ($|K| \sim 0.9$) are found for $s = 1$, which suggests that baroclinic instability of eastward flows is much more effective in terms of the spontaneous generation of LEDPs.

5. The anatomy of counter-gradient momentum transport

The ability of the multiscale model to reproduce eddy viscosity (figures 6 and 7) opens an attractive opportunity to (i) examine various processes involved in the selection of K, (ii) identify the dominant balances realized at each order in the
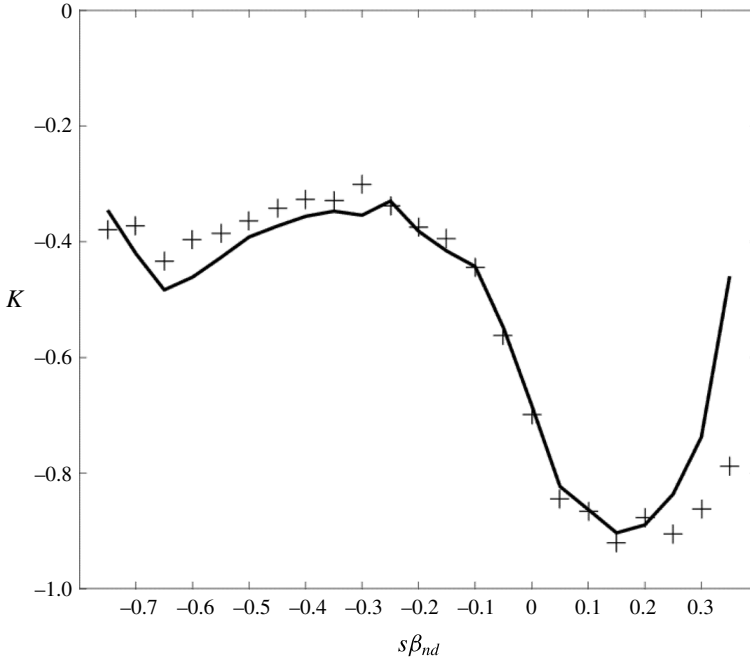
FIGURE 7. The effective eddy viscosity (K) diagnosed from numerical simulations (solid curve) is plotted as a function of $s\beta_{nd}$ along with the corresponding theoretical estimate based on the ensemble-averaged multiscale model (plus signs).

asymptotic expansion and (iii) physically interpret the chain of events leading to counter-gradient momentum transport.

The first question arising after inspection of (3.7) is the relative contributions of displacement-induced and shear-induced perturbations in the top/bottom layers to the net eddy viscosity $K_{inst} = K_1^{(1)} + K_1^{(2)} + K_2^{(1)} + K_2^{(2)}$, where

$$
\left.
\begin{aligned}
K_1^{(1)} &= -\frac{r}{1+r}\left\langle \frac{\partial \bar{\psi}_1}{\partial x}\tilde{\psi}_1^{(1)}\right\rangle, \quad
K_1^{(2)} = -\frac{2r}{1+r}\left\langle \frac{\partial \bar{\psi}_1}{\partial x}\frac{\partial \tilde{\psi}_1^{(2)}}{\partial y}\right\rangle, \\
K_2^{(1)} &= -\frac{1}{1+r}\left\langle \frac{\partial \bar{\psi}_2}{\partial x}\tilde{\psi}_2^{(1)}\right\rangle, \quad
K_2^{(2)} = -\frac{2}{1+r}\left\langle \frac{\partial \bar{\psi}_2}{\partial x}\frac{\partial \tilde{\psi}_2^{(2)}}{\partial y}\right\rangle.
\end{aligned}
\right\}
\tag{5.1}
$$

These components were evaluated from the ensemble-averaged simulation in figure 6. The values of the eddy viscosity components (5.1) recorded during the period of eddy adjustment to the large-scale forcing ($\tau = 2$) and during the quasi-equilibrium stage ($\tau = 10$) are listed in table 1. In both regimes, the dominant component of (3.6), which controls the magnitude and sign of eddy viscosity, is the upper-layer displacement term $K_1^{(1)} < 0$. The lower-layer displacement term $K_2^{(1)}$ is also negative, but it is much weaker and therefore plays a secondary role in LEDP generation. The upper- and lower-layer shearing terms ($K_{1,2}^{(2)}$) are both positive and act to reduce the counter-gradient flux driven by the upper-layer displacement mode ($K_1^{(1)}$). It should

Component	$\tau = 2$	$\tau = 10$
$K_1^{(1)}$	−1.8483	−8.6285
$K_2^{(1)}$	−0.2644	−1.2467
$K_1^{(2)}$	1.1784	7.8098
$K_2^{(2)}$	0.2562	1.2062
Total	−0.6780	−0.8592

TABLE 1. Components of the ensemble-averaged eddy viscosity from the multiscale model at the adjustment ($\tau = 2$) and the equilibrium ($\tau = 10$) stages. The dominant contributor to eddy viscosity is the displacement-driven upper-layer component $K_1^{(1)}$.

be noted, however, that the magnitude of the amplifying terms ($K_{1,2}^{(1)}$) is close to that of the stabilizing components ($K_{1,2}^{(2)}$). Thus, even small variations in each of the four terms in (5.1) could change the sign of the net viscosity.

To explain the origin of negative viscosity, we focus on the first auxiliary problem (A 9), which governs the destabilizing displacement mode. First, we note that the exact analytical solution of (A 9) is given by

$$\tilde{\psi}_i^{(1)} = \frac{\partial \bar{\psi}_i}{\partial x}(t - t_0), \quad i = 1, 2. \tag{5.2}$$

The validity of (5.2) can be readily ascertained by differentiating the governing equations for the primary eddies in x, multiplying the result by $(t - t_0)$ and subtracting from the corresponding first auxiliary equations. The physical interpretation of (5.2) is also straightforward: at the leading order, the large-scale perturbation results in the kinematic shift of the eddy pattern. Despite linear instability of the first auxiliary problem, the analytical solution (5.2) was found to be close to the corresponding numerical realizations. The relative differences between the analytical and numerical solutions accumulating over the finite integration interval $\Delta T = 25$ were of the order of 0.2 %.

The structure of the first auxiliary solution (5.2) yields insight into the mechanisms controlling the meridional potential vorticity flux associated with the displacement mode. The perturbation PV flux associated with the displacement mode in each layer contains two distinct components – advection of the basic PV by the perturbation velocity $\langle \bar{q}_i v_i^{(1)} \rangle$ and advection of the perturbation PV by the basic eddy velocity $\langle q_i^{(1)} \bar{v}_i \rangle$, where $i = 1, 2$. However, it is argued in the Appendix that $\langle \bar{q}_i v_i^{(1)} \rangle$ does not contribute to the net PV flux and the relevant component is $F_{qi}^{(1)} = \langle q_i^{(1)} \bar{v}_i \rangle$. Furthermore, at the leading order, this flux reduces to

$$F_{qi}^{(1)} = \varepsilon^3 \left\langle \frac{\partial \bar{\psi}_i}{\partial x} \tilde{\psi}_i^{(1)} \right\rangle \frac{\partial^3 \psi^{(0)}}{\partial Y^3}. \tag{5.3}$$

In view of (5.2), PV fluxes in both layers are positively correlated with $(\partial q^{(0)}/\partial Y)$, where $q^{(0)} = (\partial^2 \psi^{(0)}/\partial Y^2)$ is the vorticity of the large-scale flow. Therefore, we conclude that the sign of the depth-weighted vertical average of the PV fluxes in both layers, $F_q = (rF_{q1}^{(1)} + F_{q2}^{(1)})/(1 + r)$, is also controlled by the direction of the
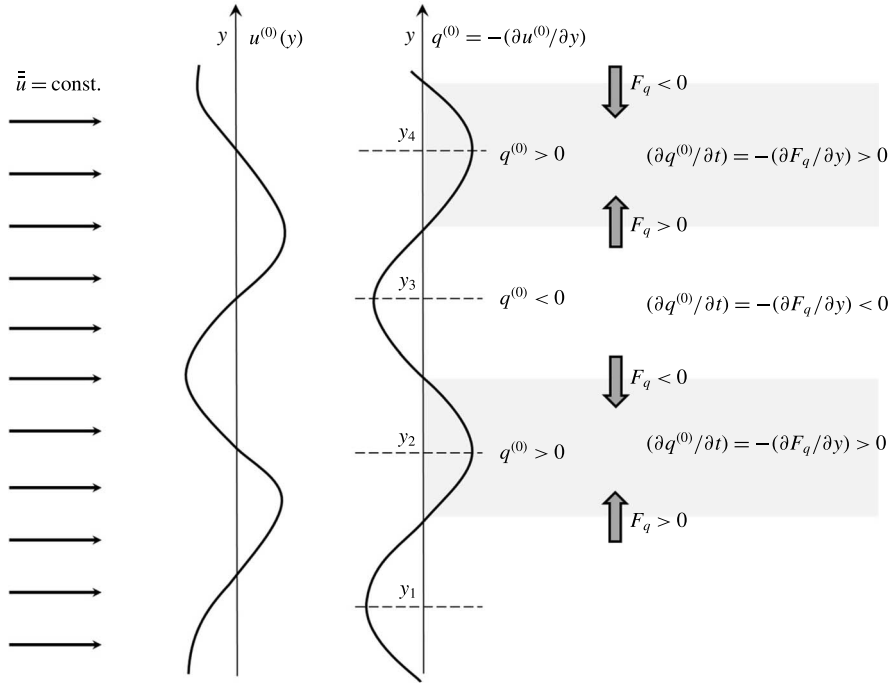
FIGURE 8. Schematic diagram illustrating the acceleration of a large-scale zonal flow by eddies. Extrema of the large-scale vorticity are indicated by y_i. The regions where the large-scale vorticity is positive are indicated by shading. The multiscale model – see (3.1a,b) – suggests that the eddy PV flux (F_q) increases with the PV gradient ($\partial q_0/\partial y$). Therefore, we expect that the divergence/convergence of fluxes will further increase the vorticity in the regions where it is already positive ($q^{(0)} > 0$) and reduce it where it is negative ($q^{(0)} < 0$).

large-scale vorticity gradient:

$$\left.\begin{aligned} F_q > 0 \quad \text{for} \quad \frac{\partial q^{(0)}}{\partial y} > 0, \\ F_q < 0 \quad \text{for} \quad \frac{\partial q^{(0)}}{\partial y} < 0. \end{aligned}\right\} \tag{5.4}$$

Thus, the barotropic vorticity flux is up-gradient, which results in the amplification of LEDPs. The physical mechanism of amplification is illustrated in figure 8, which depicts the large-scale zonal current ($\bar{\bar{u}} + u^{(0)}$) with y-dependent velocity and the corresponding vorticity pattern $q^{(0)} = -(\partial u^{(0)}/\partial y)$. According to (3.1$a,b$), the meridional eddy-induced PV flux is positive for $y_1 < y < y_2$, $y_3 < y < y_4$ and negative for $y_2 < y < y_3$, where the y_i denote the extrema of the large-scale vorticity. Thus, the divergence of the potential vorticity flux (($\partial F_q/\partial y) > 0$) results in the reduction of potential vorticity in the regions where the large-scale potential vorticity is already negative ($q^{(0)} < 0$). In regions where the large-scale potential vorticity is positive, it will be further increased. This positive feedback mechanism explains the eddy-induced amplification of large-scale perturbations and the associated negative eddy viscosity.

6. Conditions for the spontaneous generation of LEDPs

The success of the multiscale model in reproducing numerical results raises the question of whether it can also be used to explain the spontaneous emergence of LEDPs in certain regions of the parameter space and the lack of them in others (e.g. figure 4). The formation of LEDPs in simulations is apparently controlled by the competition between the destabilizing action of mesoscale eddies and the stabilizing tendency of the bottom drag acting directly on large scales. The following analysis attempts to identify and rationalize the onset of the LEDP-favourable regime as the bottom drag is gradually decreased from relatively high values, sufficient to stabilize large-scale perturbations, towards marginally unstable conditions.

The multiscale analysis (§§ 4 and 5) suggests that the effects of mesoscale eddies on the barotropic zonal current $u^{(0)}(y)$ can be represented by negative eddy viscosity (3.6). The impact of the bottom drag can be assessed by vertically averaging the governing equations (2.2), which in the absence of eddies amounts to $(\partial u^{(0)}/\partial t) = -(\gamma_{nd}/(1+r))u^{(0)}$. Assuming that the net effect can be estimated by linearly adding the two tendencies, the evolutionary equation for the large-scale flow reduces to

$$\frac{\partial u^{(0)}}{\partial t} = K\frac{\partial^2 u^{(0)}}{\partial y^2} - \frac{\gamma_{nd}}{1+r}u^{(0)}. \tag{6.1}$$

The existing evidence suggests that the linearly most unstable LEDPs take the form of zonal jets. This property is clearly revealed by numerical simulations (e.g. Berloff *et al.* 2009) and can be attributed to the generic tendency of the beta-effect to suppress large-scale meridional displacements. Therefore, it is reasonable to assume that the point of destabilization of large-scale zonal modes represents the transition between LEDP-dominated and mesoscale-dominated regimes.

The stability of large-scale zonal flows is analysed using the linear model (6.1). The substitution of normal modes $u^{(0)} = A\exp(imy + \lambda t)$ in (6.1) reveals that for $K < 0$, the large-scale flow is stable at relatively long wavelengths ($m < m_0$) and unstable at short ones ($m > m_0$), where

$$m_0 = \sqrt{-\frac{\gamma_{nd}}{K(1+r)}}. \tag{6.2}$$

If mesoscale eddies are contained within the range $m > m_{cr}$, then the condition for spontaneous formation of LEDPs becomes

$$m_0 < m_{cr}. \tag{6.3}$$

If (6.3) is satisfied, then there is a finite range of sufficiently long wavelengths $m_0 < m < m_{cr}$ that are unstable and therefore are likely to amplify.

The criterion (6.3) was used to formulate an algorithm for identifying the regions in the parameter space $(s\beta_{nd}, \gamma_{nd})$ that are susceptible to spontaneous LEDP generation as follows. We have assumed (§ 2) that the separation between meso- and large scales occurs at a wavelength $L_{cr} = 20$, and therefore the transitional wavenumber is $m_{cr} = (2\pi/L_{cr}) = 0.314$. For any given value of $s\beta_{nd}$, we performed a series of calculations in which bottom drag (assumed here to be uniform at all scales) was systematically decreased. The experiments started from a sufficiently large initial value ($\gamma_{nd} = 0.5$), which ensures that the eddy field is mesoscale-dominated. For each γ_{nd}, we evaluated the eddy viscosity K using the multiscale model and computed m_0 from (6.2). As γ_{nd} was decreased, m_0 decreased as well. Eventually, m_0 reached

the mesoscale/large-scale threshold (m_{cr}), at which point the calculation was stopped. Further decrease in γ_{nd} would imply the existence of a finite range of long unstable wavelengths ($m_0 < m < m_{cr}$). Therefore, the critical value of the bottom drag coefficient (γ_{cr}) for which $m_0 = m_{cr}$ was assumed to represent the point of transition between the mesoscale- and LEDP-dominated regimes. This procedure was repeated for a series of $s\beta_{nd}$, and the relation $\gamma_{cr}(s\beta_{nd})$ obtained in this manner is shown by the heavy curve in figure 4. The theoretical curve is in general agreement with the numerics, indicating that the LEDP-dominated region lies at relatively low values of β_{nd} and γ_{nd}. The ability of the proposed model to reproduce conditions for the spontaneous emergence of LEDPs in simulations is suggestive. It lends credence to all theoretical elements on which the algorithm is based, most notably the idea of competition between stabilizing bottom drag and destabilizing negative eddy viscosity (6.1), multiscale analysis, and the criterion for LEDP formation in (6.3).

7. Discussion

The ability of nonlinear mesoscale eddies in the ocean to excite and maintain motions on much larger spatial and temporal scales is well known (e.g. LaCasce & Pedlosky 2004; Berloff *et al.* 2009). However, specific mechanisms for the generation of LEDPs have not been fully explained. Two dominant conceptual frameworks view such phenomena as a consequence of either (i) the upscale energy cascade in two-dimensional turbulence (Kraichnan 1967; Kraichnan & Montgomery 1980; Rhines 1994) or (ii) modulational instability of mesoscale eddy patterns (Lorenz 1972; Cushman-Roisin *et al.* 1984; Gama *et al.* 1994; Manfroi & Young 1999, 2002; Connaughton *et al.* 2010). An attractive feature of the modulational stability analysis is its dynamic transparency. Explicit knowledge of the response of small-scale variability to large-scale forcing (shear and displacement in our case) makes it possible to trace and physically interpret the chain of events leading to modification of large-scale patterns by eddies.

While the extant multiscale homogenization theories undoubtedly yield important physical insights into the problem, quantitative and testable descriptions of the flow evolution are more difficult to come by. So far, the application of modulational stability models, which are usually couched in terms of multiscale analyses, has been hampered by the sensitive dependence of large-scale solutions to the assumed structure of individual eddies. The major differences in model predictions (Gama *et al.* 1994; Novikov & Papanicolau 2001; Radko 2011*a*,*c*) underscore the importance of the chosen background eddy pattern. Our present study attempts to address this complication by using the time-dependent background obtained directly from simulations of mesoscale eddies – the approach referred to as the AE model. The resulting mesoscale field is representative and dynamically consistent, which holds the promise of producing sufficiently accurate large-scale evolutionary equations.

The initial application of the AE multiscale analysis to the two-layer model of baroclinic instability (Phillips 1951) has been encouraging. The evolutionary equation suggested by the multiscale model takes the form of the diffusion equation (3.5) with negative coefficient K. The multiscale theory made it possible to evaluate the effective eddy viscosity and its variation with background parameters, which was subsequently confirmed by direct numerical simulations. In this regard, we should mention the recent work of Jansen & Held (2014) and Jansen *et al.* (2015), who use a negative-viscosity formulation to represent subgrid eddy effects in models of geostrophic ocean turbulence. The success of the negative-viscosity parameterization

reported in these studies is consistent with the theoretical results presented here. On the other hand, Srinivasan & Young (2012) examined the spontaneous formation of zonal jets in the barotropic model with isotropic noise forcing and suggested that the growth of jets is associated with a destabilizing hyper-viscous term, rather than with the negative-viscosity mechanism considered here. The ultimate cause of the disagreement remains to be identified.

One of the key strengths of multiscale analysis lies in its explicit treatment of interactions between flow components operating on dissimilar scales. This transparency has been exploited here to identify the dominant balances in the multiscale expansion and to accordingly interpret the dynamics of counter-gradient momentum flux by mesoscales. We have argued that precise conditions for the emergence of large scales in our model are set by the competition between the destabilizing influence of background eddies and the stabilizing tendency of bottom drag acting directly on large-scale flows. This balance is a key feature of the simple dynamical model (§ 6) which is designed to explain the emergence of LEDPs in simulations.

Despite the ability of the multiscale model to rationalize numerical results, it is perhaps premature at this point to argue that the modulational instability view of LEDP generation should be given priority over its alternative interpretation as an upscale cascade of energy. In fact, our results suggest that the modulational instability and cascade-based theories should not be viewed as mutually exclusive. According to the multiscale model, the wavelengths characterized by the largest growth rates – and therefore most likely to amplify first – are relatively moderate. Hence, the successive coalescences of LEDPs into larger and larger structures could indeed play an important role in the unconstrained evolution of baroclinically unstable systems. In principle, sequential interactions, which are not accounted for in the present minimal version of the AE theory, can be represented by the iterative application of multiscale models from one range of scales to the next (cf. Bensoussan, Lions & Papanicolaou 1978).

Another caveat of the presented analysis is related to the identification of LEDPs. While the theoretical multiscale model *a priori* assumes asymptotic scale separation between primary mesoscale variability and amplifying large scales, diagnostics of fully nonlinear simulations and/or field data are less straightforward. In this study, LEDP-susceptible parameters in numerical experiments (figure 4) were determined using a convenient but perhaps overly simplistic criterion based on the relative amount of energy contained in Fourier components with wavelengths exceeding a critical value. The critical wavelength was assumed to be independent of the governing parameters and was chosen somewhat arbitrarily to be $L_{cr} = 20$. Although even such a crude criterion has led to qualitatively consistent results, the development of a more objective and configuration-dependent operational definition of LEDPs would undoubtedly enhance the accuracy and generality of our analysis.

The multiscale AE model could also be extended in a number of other directions. It is highly desirable to move beyond the special case of zonally uniform LEDPs and explain their two-dimensional dynamics and nonlinear amplitude equilibration. The primary purpose of the present model is to explain the onset of the LEDP-dominated regime. Since zonal modes represent the most rapidly amplifying (or the least damped) large-scale perturbations, this objective was accomplished by focusing exclusively on zonal jets. However, further reduction in the bottom drag will result in transition to the strongly unstable regime characterized by the appearance of amplifying non-zonal large-scale modes and their nonlinear interaction. In this regard, it should be mentioned that the parameter regime relevant for the Earth's oceans is

perhaps only weakly unstable with regard to the spontaneous formation of LEDPs (e.g. Berloff *et al.* 2011), which makes the present form of the multiscale model directly applicable. However, more active systems, characterized by the effective absence of bottom drag, such as realized in the atmospheres of giant planets, would require a significant revision and reassessment of the present multiscale model.

Relatively straightforward changes to the model formulation would make it possible to take into account topographic influences, external forcing and arbitrary orientations of the mean background flow. Inclusion of pre-existing large-scale variability into the model would allow analysis of spatially inhomogeneous eddy viscosity and its effects on the LEDP dynamics. Extension of the asymptotic expansion (3.3) to higher orders may lead to an amplitude equation of Cahn–Hilliard type (Cahn & Hilliard 1958) in which the destabilizing tendency of negative viscosity is counteracted, at moderate scales, by the dissipative fourth-order operator. The inclusion of high-order dissipative processes, in turn, would open the pathway for theoretical investigations of the preferred length scales of LEDPs.

Another promising route would be to further improve the analytical tractability of the proposed multiscale analysis. The AE model uses numerically derived background eddy patterns, and its success can guide the selection of adequate analytical approximations of mesoscale variability. The theory of coherent mesoscale vortices is relatively well developed (Nof 1981, 1983; Sutyrin & Dewar 1992; Reznik & Dewar 1994; Radko & Stern 1999, 2000; Benilov 2000; among many others). Models of this type represent the dynamics of individual eddies, and multiscale analysis opens an attractive opportunity to describe the cumulative effect of vortex arrays on large-scale circulation patterns.

Finally, there is no reason to limit such multiscale investigations to baroclinic instability. We anticipate that similar analyses should be applicable to a wide range of small-scale phenomena known to generate structures on scales greatly exceeding that of primary modes. For instance, an obvious candidate for application of the multiscale AE model is double-diffusive convection (Stern 1960). The latter is a form of instability operating on a centimetre scale in the ocean, which nevertheless generates secondary structures (thermohaline staircases and intrusions) that extend tens and hundreds of metres vertically. Multiscale models are well suited for linking individual and collective aspects of eddy dynamics, both of which are essential for understanding the interactions of spatially and temporally dissimilar structures – interactions that are very common in fluid mechanics.

Appendix. Details of multiscale analysis

We are concerned by the ability of relatively small-scale eddies, represented by the streamfunction fields $\bar{\psi}_{1,2}(x, y, t)$, to affect the slow evolution of a large-scale zonal flow. The interaction between vastly dissimilar flow components is described using new spatial variables (T, Y) over which the background pattern is modulated. The new variables are scaled relative to the old variables according to (3.2). In this regard, it should be noted that the choice of the temporal/spatial sector for scaling of large-scale variables is neither unique nor obvious. Depending on the

particular problem – governing equations and background small-scale pattern – the asymptotic dependences of the time scale can be very different. For instance, the relevant scaling can be linear (in ε) in both space and time, as in the anisotropic kinetic alpha (AKA) effect (Frisch *et al.* 1987; Sulem *et al.* 1989). Certain inviscid systems are characterized by the appearance of 'eddy-explosion' modes (Radko 2011*a*), operating in the temporal/spatial sector $(\partial/\partial t, \partial/\partial x) \sim (\varepsilon, \varepsilon^2)$. However, the numerical simulations in §2 indicate that the growth rate of unstable large-scale modes is proportional to their wavenumber squared (e.g. figure 3*b*). This suggests that representative asymptotic solutions will be found in the sector $(\partial/\partial t, \partial/\partial x) \sim (\varepsilon^2, \varepsilon)$. Therefore, the most conventional scaling (3.2) applies, which holds the promise of an unambiguous calculation of eddy viscosity.

The search for specific large-scale solutions is based on the following conventional steps:

(i) (x, y, Y, t, T) are treated as independent variables;

(ii) the spatial and temporal derivatives in the linear system are replaced as

$$\frac{\partial}{\partial t} \to \frac{\partial}{\partial t} + \varepsilon^2 \frac{\partial}{\partial T}, \ \frac{\partial}{\partial y} \to \frac{\partial}{\partial y} + \varepsilon \frac{\partial}{\partial Y}; \tag{A 1}$$

(iii) the governing equations (2.2) are linearized with respect to the background state $\bar{\psi}_{1,2}(x, y, t)$;

(iv) the perturbation solution is sought as a series in ε,

$$\psi'_i = \psi_i^{(0)} + \varepsilon \psi_i^{(1)} + \varepsilon^2 \psi_i^{(2)} + \cdots, \quad i = 1, 2. \tag{A 2}$$

To isolate the effects of eddies in the generation of LEDPs, we temporarily ignore the effects of bottom drag on the large-scale flow. This will make it possible to quantify the destabilizing tendencies of mesoscale eddies, which will be *a posteriori* compared with the stabilizing tendency of bottom drag (§6). To represent the eddy-induced evolution of a large-scale zonal flow, the expansion opens with the leading-order term which varies only on large temporal and spatial scales. However, when $\psi_{1,2}^{(0)}$ are taken to be arbitrary functions of (Y, T), the averaging of the second order balances of governing equations in (x, y) leads to the following solvability condition:

$$\frac{\partial}{\partial T}(\psi_1^{(0)} - \psi_2^{(0)}) = 0. \tag{A 3}$$

Equation (A 3) implies that all amplifying large-scale modes are necessarily barotropic: $\psi_1^{(0)} = \psi_2^{(0)}$. This condition is consistent with the numerical results (e.g. figure 2) and provides a formal rationalization of the predominantly barotropic character of LEDPs. To streamline the exposition, we assume from the outset that

$$\psi_{1,2}^{(0)} = \psi^{(0)}(Y, T). \tag{A 4}$$

Next, we substitute series (A 2) in the linearized quasi-geostrophic system, collect terms of the same order in ε and sequentially solve the resulting hierarchy of systems until a closed equation for $\psi^{(0)}$ is obtained. The first order equation takes the form

$$A \begin{pmatrix} \psi_1^{(1)} \\ \psi_2^{(1)} \end{pmatrix} = \frac{\partial \psi^{(0)}}{\partial Y} \begin{pmatrix} \dfrac{\partial \bar{q}_1}{\partial x} \\ \dfrac{\partial \bar{q}_2}{\partial x} \end{pmatrix}, \tag{A 5}$$

where $\bar{q}_1 = \nabla^2 \bar{\psi}_1 + (\bar{\psi}_2 - \bar{\psi}_1)$ and $\bar{q}_2 = \nabla^2 \bar{\psi}_2 + r(\bar{\psi}_1 - \bar{\psi}_2)$. The linear homogeneous differential operator A is defined as follows:

$$
A \begin{pmatrix} \phi_1 \\ \phi_2 \end{pmatrix} \equiv \begin{pmatrix} \dfrac{\partial f_1}{\partial t} + J(\phi_1, \bar{q}_1) + J(\bar{\psi}_1, f_1) + (\beta_{nd} + s)\dfrac{\partial \phi_1}{\partial x} + s\dfrac{\partial f_1}{\partial x} - \nu_{nd}\nabla^4 \phi_1 \\[2ex] \dfrac{\partial f_2}{\partial t} + J(\phi_2, \bar{q}_2) + J(\bar{\psi}_2, f_2) + (\beta_{nd} - sr)\dfrac{\partial \phi_2}{\partial x} + \gamma_{nd}\nabla^2 \phi_2 - \nu_{nd}\nabla^4 \phi_2 \end{pmatrix},
$$

$$(A\,6)$$

and

$$
f_1 = \nabla^2 \phi_1 + (\phi_2 - \phi_1), \quad f_2 = \nabla^2 \phi_2 + r(\phi_1 - \phi_2). \tag{A 7a,b}
$$

Noticing that the operator A involves only the small-scale spatial variables, we solve (A 5) by introducing new variables $(\tilde{\psi}_1^{(1)}, \tilde{\psi}_2^{(1)})$ such that

$$
\psi_i^{(1)} = \frac{\partial \psi_0}{\partial Y} \tilde{\psi}_i^{(1)}, \quad i = 1, 2. \tag{A 8}
$$

Substitution of (A 8) into the first-order equation (A 5) produces an inhomogeneous linear equation

$$
A \begin{pmatrix} \tilde{\psi}_1^{(1)} \\ \tilde{\psi}_2^{(1)} \end{pmatrix} = \begin{pmatrix} \dfrac{\partial \bar{q}_1}{\partial x} \\[2ex] \dfrac{\partial \bar{q}_2}{\partial x} \end{pmatrix}, \tag{A 9}
$$

which contains no reference to large-scale variables and therefore can be solved for $\tilde{\psi}_{1,2}^{(1)}(x, y, t)$, which are referred to as the auxiliary functions of the first order. Solutions of the first auxiliary problem represent the leading-order response of mesoscale eddies to the x-displacement induced by the large-scale current.

Extending the expansion to the second order, we similarly arrive at the second auxiliary problem:

$$
A \begin{pmatrix} \tilde{\psi}_1^{(2)} \\ \tilde{\psi}_2^{(2)} \end{pmatrix}
$$
$$
= \begin{pmatrix} \tilde{\psi}_1^{(1)} \dfrac{\partial}{\partial x}\bar{q}_1 - \dfrac{\partial}{\partial x}\bar{\psi}_1 \tilde{q}_1^{(1)} - 2J\left(\bar{\psi}_1, \dfrac{\partial}{\partial y}\tilde{\psi}_1^{(1)}\right) - 2\dfrac{\partial^2}{\partial x \partial y}\tilde{\psi}_1^{(1)} + 4\nu_{nd}\dfrac{\partial}{\partial y}\nabla^2 \tilde{\psi}_1^{(1)} - 2\dfrac{\partial^2}{\partial t \partial y}\tilde{\psi}_1^{(1)} \\[2ex] \tilde{\psi}_2^{(1)} \dfrac{\partial}{\partial x}\bar{q}_2 - \dfrac{\partial}{\partial x}\bar{\psi}_2 \tilde{q}_2^{(1)} - 2J\left(\bar{\psi}_2, \dfrac{\partial}{\partial y}\tilde{\psi}_2^{(1)}\right) + 4\nu_{nd}\dfrac{\partial}{\partial y}\nabla^2 \tilde{\psi}_2^{(1)} - 2\dfrac{\partial^2}{\partial t \partial y}\tilde{\psi}_2^{(1)} - 2\gamma_{nd}\dfrac{\partial}{\partial y}\tilde{\psi}_2^{(1)} \end{pmatrix},
$$

$$(A\,10)$$

where

$$
\psi_i^{(2)} = \frac{\partial^2 \psi^{(0)}}{\partial Y^2} \tilde{\psi}_i^{(2)}, \quad i = 1, 2. \tag{A 11}
$$

This system also does not involve large-scale variables and therefore can be solved for $\tilde{\psi}_{1,2}^{(2)}(x, y, t)$. Solutions of the second auxiliary problem reflect the modification of eddies by the shear imposed by the large-scale current.

Although the third-order balance can be treated in a similar fashion, it can be shown (Gama *et al.* 1994; Novikov & Papanicolau 2001) that it plays no role in the derivation of the closed large-scale model. The final condition results from the

fourth-order equation, which is averaged in small-scale variables (x, y, t) and vertically over the depths of the two layers:

$$\frac{\partial^3 \psi^{(0)}}{\partial T \partial Y^2} = -\frac{1}{1+r} \frac{\partial^4 \psi^{(0)}}{\partial Y^4} \left[\left\langle r \frac{\partial \bar{\psi}_1}{\partial x} \left(2\frac{\partial \tilde{\psi}_1^{(2)}}{\partial y} + \tilde{\psi}_1^{(1)} \right) + \frac{\partial \bar{\psi}_2}{\partial x} \left(2\frac{\partial \tilde{\psi}_2^{(2)}}{\partial y} + \tilde{\psi}_2^{(1)} \right) \right\rangle \right]$$
$$+ \nu_{nd} \frac{\partial^4 \psi_0}{\partial Y^4}. \tag{A 12}$$

The angular brackets in (A 12) represent averaging in x and y, and the square brackets represent averaging in time, over a period exceeding the typical eddy scale. Equation (A 12) represents a closed equation for the leading-order large-scale component, and it is written in terms of rescaled large-scale units (Y, T). At this point, the multiscale analysis is complete and we can revert to the original spatial and temporal variables y and t using (3.2) without the risk of confusing the scales. The effects of explicit lateral friction, represented by the last term in (A 12), are weak and could be ignored for most intents and purposes. When the result is integrated in y, we discover that the evolution of the large-scale flow is governed by the diffusion equation

$$\frac{\partial}{\partial t} u^{(0)} = K \frac{\partial^2}{\partial y^2} u^{(0)}, \tag{A 13}$$

where $u^{(0)} = -(\partial \psi^{(0)} / \partial y)$ is the zonal velocity of the large-scale flow and

$$K = -\frac{1}{1+r} \left[\left\langle r \frac{\partial \bar{\psi}_1}{\partial x} \left(2\frac{\partial \tilde{\psi}_1^{(2)}}{\partial y} + \tilde{\psi}_1^{(1)} \right) + \frac{\partial \bar{\psi}_2}{\partial x} \left(2\frac{\partial \tilde{\psi}_2^{(2)}}{\partial y} + \tilde{\psi}_2^{(1)} \right) \right\rangle \right]. \tag{A 14}$$

Based on (A 13), we readily interpret K as the effective eddy viscosity.

The physical interpretation of the individual eddy viscosity components in (A 14) warrants some further discussion. Equation (A 12) represents averaging of the governing equations in (x, y) and depth-weighted averaging of the result over two layers. The nonlinear terms on the right-hand side of (A 12) originate from the advective (Jacobian) terms in (2.2). These components could be expressed as

$$M = \left\langle \frac{r}{1+r} (J_{xy}(\psi_1, q_1) + \varepsilon J_{xY}(\psi_1, q_1)) + \frac{1}{1+r} (J_{xy}(\psi_2, q_2) + \varepsilon J_{xY}(\psi_2, q_2)) \right\rangle, \tag{A 15}$$

where

$$\left. \begin{aligned} q_1 &= \frac{\partial^2 \psi_1}{\partial x^2} + \frac{\partial^2 \psi_1}{\partial y^2} + 2\varepsilon \frac{\partial^2 \psi_1}{\partial y \partial Y} + \varepsilon^2 \frac{\partial^2 \psi_1}{\partial Y^2} + (\psi_2 - \psi_1), \\ q_2 &= \frac{\partial^2 \psi_2}{\partial x^2} + \frac{\partial^2 \psi_2}{\partial y^2} + 2\varepsilon \frac{\partial^2 \psi_2}{\partial y \partial Y} + \varepsilon^2 \frac{\partial^2 \psi_2}{\partial Y^2} + r(\psi_1 - \psi_2). \end{aligned} \right\} \tag{A 16}$$

Since the (x, y) average of $J_{xy}(\psi_i, q_i)$ is zero, (A 15) reduces to

$$M = \varepsilon \frac{\partial}{\partial Y} \left\langle \frac{r}{1+r} \frac{\partial \psi_1}{\partial x} q_1 + \frac{1}{1+r} \frac{\partial \psi_2}{\partial x} q_2 \right\rangle, \tag{A 17}$$

which is readily interpreted as the large-scale meridional convergence of the depth-averaged meridional PV fluxes F_{qi}, where

$$F_{qi} = \langle v_i q_i \rangle = \left\langle \frac{\partial \psi_i}{\partial x} q_i \right\rangle, \quad i = 1, 2. \tag{A 18}$$

When (3.3) and (A 16) are used to express (A 17) in terms of various streamfunction components, it becomes apparent that at the leading order ($\sim \varepsilon^4$) it contains four clearly identifiable flux terms:

$$
M \approx \varepsilon \frac{\partial}{\partial Y} \left\langle \frac{r}{1+r} \frac{\partial \bar{\psi}_1}{\partial x} q_1^{(1)} + \frac{1}{1+r} \frac{\partial \bar{\psi}_2}{\partial x} q_2^{(1)} + \frac{r}{1+r} \frac{\partial \bar{\psi}_1}{\partial x} q_1^{(2)} + \frac{1}{1+r} \frac{\partial \bar{\psi}_2}{\partial x} q_2^{(2)} \right\rangle, \quad \text{(A 19)}
$$

where $q_i^{(j)}$ is the potential vorticity associated with streamfunction components $\psi_i^{(j)}$. For instance, diagnostics of the numerical solutions (§ 5) indicate that the amplification of the large-scale jets is driven by the displacement mode, and the associated flux component is given by

$$
F_{qi}^{(1)} = \varepsilon \left\langle \frac{\partial \bar{\psi}_i}{\partial x} q_i^{(1)} \right\rangle. \quad \text{(A 20)}
$$

It should be emphasized that (A 20) represents the advection of perturbation PV ($q_i^{(1)}$) by the meridional velocity of primary eddies ($\bar{v}_i = (\partial \bar{\psi}_i / \partial x)$). One might intuitively expect that the net PV flux contains comparable contributions from the advection of primary PV by perturbation velocity and the advection of perturbation PV by the primary velocity. However, the former term does not appear, at the leading order, in the flux divergence term M. While this result follows directly from the asymptotic expansion, it is of interest to explore its physical origin. One of the explanations can be given in terms of Galilean invariance. In particular, we can insist that integral properties of our solution cannot change if the total flow field is displaced in the zonal direction with uniform velocity. Therefore, the meridional PV flux is invariant under the transformation

$$
\psi^{(0)} \rightarrow \psi^{(0)} + AY, \quad \text{(A 21)}
$$

where A can be any constant. The flux component representing advection of primary PV by the perturbation velocity in the displacement-induced mode is

$$
F_{qiA}^{(1)} = \varepsilon \left\langle \bar{q}_i \frac{\partial \tilde{\psi}_i^{(1)}}{\partial x} \right\rangle \frac{\partial \psi_0}{\partial Y}. \quad \text{(A 22)}
$$

However, the invariance of our solutions with respect to (A 21) implies that all flux components involving the first derivative of $\psi^{(0)}$ have to vanish in the integral sense. This is only possible if the coefficient $\langle \bar{q}_i (\partial \tilde{\psi}_i^{(1)} / \partial x) \rangle$ is identically zero, which implies that $F_{qiA}^{(1)} = 0$. For the flux component associated with the advection of the perturbation PV, no such restriction arises because it contains higher derivatives of $\psi^{(0)}$ that are invariant with respect to (A 21). The multiscale model (A 14) indicates that the only flux component of the displacement-induced mode $F_{qi}^{(1)}$ that ultimately contributes to the eddy viscosity term is given by

$$
F_{qiB}^{(1)} = \varepsilon^3 \frac{\partial \bar{\psi}}{\partial x} \frac{\partial^3 \psi^{(0)}}{\partial Y^3} \tilde{\psi}_i^{(1)}. \quad \text{(A 23)}
$$

REFERENCES

BALMFORTH, N. J. & YOUNG, Y.-N. 2002 Stratified Kolmogorov flow. *J. Fluid Mech.* **450**, 131–167.

BALMFORTH, N. J. & YOUNG, Y.-N. 2005 Stratified Kolmogorov flow. Part 2. *J. Fluid Mech.* **528**, 23–42.

BENILOV, E. S. 2000 The dynamics of a near-surface vortex in a two-layer ocean on the beta-plane. *J. Fluid Mech.* **420**, 277–299.

BENSOUSSAN, A., LIONS, J. & PAPANICOLAOU, G. 1978 *Asymptotic Analysis for Periodic Structures*. North-Holland.

BERLOFF, P., KAMENKOVICH, I. & PEDLOSKY, J. 2009 A mechanism of formation of multiple zonal jets in the oceans. *J. Fluid Mech.* **628**, 395–425.

BERLOFF, P., KARABASOV, S., FARRAR, T. & KAMENKOVICH, I. 2011 On latency of multiple zonal jets in the oceans. *J. Fluid Mech.* **686**, 534–567.

CAHN, J. W. & HILLIARD, J. E. 1958 Free energy of a nonuniform system. I: interfacial free energy. *J. Chem. Phys.* **28**, 258–267.

CHAVES, M. & GAMA, S. 2000 Time evolution of the eddy viscosity in two-dimensional Navier–Stokes flow. *Phys. Rev.* E **61**, 2118–2120.

CONNAUGHTON, C. P., NADIGA, B. T., NAZARENKO, S. V. & QUINN, B. E. 2010 Modulational instability of Rossby and drift waves and generation of zonal jets. *J. Fluid Mech.* **654**, 207–231.

CUMMINS, P. F. & HOLLOWAY, G. 2010 Reynolds stress and eddy viscosity in direct numerical simulations of sheared two-dimensional turbulence. *J. Fluid. Mech.* **657**, 394–412.

CUSHMAN-ROISIN, B., MCLAUGHLIN, D. & PAPANICOLAOU, G. 1984 Interactions between mean flow and finite-amplitude mesoscale eddies in a barotropic ocean. *Geophys. Astrophys. Fluid Dyn.* **29**, 333–353.

DRITSCHEL, D. & MCINTYRE, M. 2008 Multiple jets as PV staircases: the Phillips effect and the resilience of eddy-transport barriers. *J. Atmos. Sci.* **65**, 855–874.

FRISCH, U., LEGRAS, B. & VILLONE, B. 1996 Large scale Kolmogorov flow on the beta-plane and resonant wave interaction. *Physica* D **94**, 36–56.

FRISCH, U., SHE, Z. & SULEM, P. 1987 Large-scale flow driven by the anisotropic kinetic alpha effect. *Physica* D **28**, 382–392.

GAMA, S., VERGASSOLA, M. & FRISCH, U. 1994 Negative eddy viscosity in isotropically forced 2-dimensional flow – linear and nonlinear dynamics. *J. Fluid Mech.* **260**, 95–126.

GILLE, S. & DAVIS, R. 1999 The influence of mesoscale eddies on coarsely resolved density: an examination of subgrid-scale parameterization. *J. Phys. Oceanogr.* **29**, 1109–1123.

HELD, I. 1975 Momentum transport by quasi-geostrophic eddies. *J. Atmos. Sci.* **32**, 1494–1497.

HELD, I. M. & LARICHEV, V. D. 1996 A scaling theory for horizontally homogeneous, baroclinically unstable flow on a beta plane. *J. Atmos. Sci.* **53**, 946–952.

HUANG, H.-P. & ROBINSON, W. 1998 Two-dimensional turbulence and persistent zonal jets in a global barotropic model. *J. Atmos. Sci.* **55**, 611–632.

JANSEN, M. F., ADCROFT, A. J., HALLBERG, R. & HELD, I. M. 2015 Parameterization of eddy fluxes based on a mesoscale energy budget. *Ocean Model.* **92**, 28–41.

JANSEN, M. F. & HELD, I. M. 2014 Parameterizing subgrid-scale eddy effects using energetically consistent backscatter. *Ocean Model.* **80**, 36–48.

KAMENKOVICH, I., BERLOFF, P. & PEDLOSKY, J. 2009 Anisotropic material transport by eddies and eddy-driven currents in a model of the North Atlantic. *J. Phys. Oceanogr.* **39**, 3162–3175.

KAMENKOVICH, I., RYPINA, I. & BERLOFF, P. 2015 Properties and origins of the anisotropic eddy-induced transport in the North Atlantic. *J. Phys. Oceanogr.* **45**, 778–791.

KAMENKOVICH, V. M., KOSHLYAKOV, M. N. & MONIN, A. S. 1986 *Synoptic Eddies in the Ocean*. Springer.

KEVORKIAN, J. & COLE, J. D. 1996 *Multiple Scale and Singular Perturbation Methods*, p. 632. Springer.

KRAICHNAN, R. & MONTGOMERY, D. 1980 Two-dimensional turbulence. *Rep. Prog. Phys.* **43**, 547–619.

KRAICHNAN, R. H. 1967 Inertial ranges in two-dimensional turbulence. *Phys. Fluids* **10**, 1417–1423.

LaCasce, J. & Pedlosky, J. 2004 The instability of Rossby basin modes and the oceanic eddy field. *J. Phys. Oceanogr.* **34**, 2027–2041.

Larichev, V. D. & Held, I. M. 1995 Eddy amplitudes and fluxes in a homogeneous model of fully developed baroclinic instability. *J. Phys. Oceanogr.* **25**, 2285–2297.

Legras, B. & Villone, B. 2009 Large-scale instability of a generalized turbulent Kolmogorov flow. *Nonlinear Process. Geophys.* **16**, 569–577.

Lorenz, E. N. 1972 Barotropic instability of Rossby wave motion. *J. Atmos. Sci.* **29**, 258–269.

Manfroi, A. & Young, W. 1999 Slow evolution of zonal jets on the beta plane. *J. Atmos. Sci.* **56**, 784–800.

Manfroi, A. & Young, W. 2002 Stability of beta-plane Kolmogorov flow. *Physica* D **162**, 208–232.

Matulka, A. M. & Afanasyev, Y. D. 2015 Zonal jets in equilibrating baroclinic instability on the polar beta-plane: experiments with altimetry. *J. Geophys. Res. Oceans* **120**, 6130–6144.

Maximenko, N., Bang, B. & Sasaki, H. 2005 Observational evidence of alternating zonal jets in the world ocean. *Geophys. Res. Lett.* **32**, L12607.

McWilliams, J. C. & Chow, J. H. S. 1981 Equilibrium geostrophic turbulence. I: a reference solution in a beta-plane channel. *J. Phys. Oceanogr.* **11**, 921–949.

Mei, C. C. & Vernescu, M. 2010 *Homogenization Methods for Multiscale Mechanics*. World Scientific Publishing.

Melnichenko, O. V., Maximenko, N. A., Schneider, N. & Sasaki, H. 2010 Quasi-stationary striations in basin-scale oceanic circulation: vorticity balance from observations and eddy-resolving model. *Ocean Dyn.* **60**, 653–666.

Meshalkin, L. & Sinai, Y. 1961 Investigation of the stability of a stationary solution of a system of equations for the plane movement of an incompressible viscous fluid. *Z. Angew. Math. Mech.* **25**, 1700–1705.

Nadiga, B. 2006 On zonal jets in oceans. *Geophys. Res. Lett.* **33**, L10601.

Nadiga, B. T. & Straub, D. N. 2010 Alternating zonal jets and energy fluxes in barotropic wind-driven gyres. *Ocean Model.* **33**, 257–269.

Nakamura, M. & Chao, Y. 2000 On the eddy isopycnal thickness diffusivity of the Gent–McWilliams subgrid mixing parameterization. *J. Clim.* **13**, 502–510.

Nakano, H. & Hasumi, H. 2005 A series of zonal jets embedded in the broad zonal flows in the Pacific obtained in eddy-permitting ocean general circulation models. *J. Phys. Oceanogr.* **35**, 474–488.

Nepomnyashchy, A. 1976 On the stability of the secondary flow of a viscous fluid in an infinite domain. *Z. Angew. Math. Mech. Appl. Math. Mech.* **40**, 886–891.

Nof, D. 1981 On the beta-induced movement of isolated baroclinic eddies. *J. Phys. Oceanogr.* **11**, 1662–1672.

Nof, D. 1983 On the migration of isolated eddies with application to Gulf Stream rings. *J. Mar. Res.* **41**, 399–425.

Novikov, A. & Papanicolau, G. 2001 Eddy viscosity of cellular flows. *J. Fluid Mech.* **446**, 173–198.

Nowlin, W. & Klinck, J. 1986 The physics of the Antarctic circumpolar current. *Rev. Geophys.* **24**, 469–491.

Orsi, A. H., Whitworth, T. & Nowlin, W. 1995 On the meridional extent and fronts of the Antarctic circumpolar current. *Deep-Sea Res.* **42**, 641–673.

Pedlosky, J. 1970 Finite-amplitude baroclinic waves. *J. Atmos. Sci.* **27**, 15–30.

Pedlosky, J. 1987 *Geophysical Fluid Dynamics*. Springer.

Phillips, N. A. 1951 A simple three-dimensional model for the study of large scale extra tropical flow pattern. *J. Met.* **8**, 381–394.

Radko, T. 2011*a* On the generation of large-scale structures in a homogeneous eddy field. *J. Fluid Mech.* **668**, 76–99.

Radko, T. 2011*b* Mechanics of thermohaline interleaving: beyond the empirical flux laws. *J. Fluid Mech.* **675**, 117–140.

Radko, T. 2011*c* Eddy viscosity and diffusivity in the modon-sea model. *J. Mar. Res.* **69**, 723–752.

RADKO, T. 2014 Applicability and failure of the flux-gradient laws in double-diffusive convection. *J. Fluid Mech.* **750**, 33–72.

RADKO, T., PEIXOTO DE CARVALHO, D. & FLANAGAN, J. 2014 Nonlinear equilibration of baroclinic instability: the growth rate balance model. *J. Phys. Oceanogr.* **44**, 1919–1940.

RADKO, T. & STERN, M. E. 1999 On the propagation of oceanic mesoscale vortices. *J. Fluid Mech.* **380**, 39–57.

RADKO, T. & STERN, M. E. 2000 Self-propagating eddies on the stratifed f-plane. *J. Phys. Oceanogr.* **30**, 3134–3144.

REZNIK, G. M. & DEWAR, W. K. 1994 An analytical theory of distributed axisymmetrical barotropic vortices on the beta-plane. *J. Fluid Mech.* **269**, 301–321.

RHINES, P. B. 1977 The dynamics of unsteady currents. In *The Sea* (ed. E. A. Goldberg *et al.*), Marine Modeling, vol. 6, pp. 189–318. Wiley.

RHINES, P. B. 1994 Jets. *Chaos* **4**, 313–339.

RICHARDS, K., MAXIMENKO, N., BRYAN, F. & SASAKI, H. 2006 Zonal jets in the Pacific Ocean. *Geophys. Res. Lett.* **33**, L03605.

ROBERTS, M. & MARSHALL, D. 2000 On the validity of downgradient eddy closures in ocean models. *J. Geophys. Res.* **105**, 28613–28627.

ROBINSON, A. R. (Ed.) 1983 *Eddies in Marine Science*. Springer.

SHEPHERD, T. G. 1988 Nonlinear saturation of baroclinic instability. Part I: the two-layer model. *J. Atmos. Sci.* **45**, 2014–2025.

SIVASHINSKY, G. 1985 Weak turbulence in periodic flows. *Physica* D **17**, 243–255.

SOKOLOV, S. & RINTOUL, S. 2007 Multiple jets of the Antarctic circumpolar current south of Australia. *J. Phys. Oceanogr.* **37**, 1394–1412.

SRINIVASAN, K. & YOUNG, W. R. 2012 Zonostrophic instability. *J. Atmos. Sci.* **69**, 1633–1656.

STARR, V. P. 1968 *Physics of Negative Viscosity Phenomena*. McGraw-Hill.

STERN, M. E. 1960 The 'salt-fountain' and thermohaline convection. *Tellus* **12**, 172–175.

SULEM, P., SHE, Z., SCHOLL, H. & FRISCH, U. 1989 Generation of large-scale structures in three-dimensional flow lacking parity-invariance. *J. Fluid Mech.* **205**, 341–358.

SUTYRIN, G. G. & DEWAR, W. K. 1992 Almost symmetrical solitary eddies in a 2-layer ocean. *J. Fluid Mech.* **238**, 633–656.

THOMPSON, A. F. & YOUNG, W. R. 2006 Scaling baroclinic eddy fluxes: vortices and energy balance. *J. Phys. Oceanogr.* **36**, 720–738.

THOMPSON, A. F. & YOUNG, W. R. 2007 Two-layer baroclinic eddy heat fluxes: zonal flows and energy balance. *J. Atmos. Sci.* **64**, 3214–3231.

WIRTH, A., GAMA, S. & FRISCH, U. 1995 Eddy viscosity of three-dimensional flow. *J. Fluid Mech.* **288**, 249–264.